Variations in Subsidence along the Gulf of Mexico passive margin from Airborne-LiDAR data and Time Series InSAR in Louisiana

Carolina Hurtado-Pulido[1], Reda Amer[2], Cynthia Ebinger[1], and Hayden Holcomb[1]

[1]Tulane University
[2]Lamar University

March 07, 2024

Abstract

The Coast of Louisiana is affected by accelerating sea level rise compounded by land subsidence, leading to land loss. Vertical crustal motions in the region are caused by natural and anthropogenic processes that vary temporally and spatially across the Gulf of Mexico. We investigate the role of growth faulting contributions to subsidence in a case study of Baton Rouge, where two E-W striking, down-to-the-south normal faults, the Denham Springs and Baton Rouge faults, cut compacted Pleistocene strata, and where sediment compaction should be minimal. We used InSAR time series and LiDAR differencing data spanning 1999-2020 to quantify modern vertical and horizontal displacements. After calibration with GNSS data, both methods reveal similar spatial patterns in ground motion, with the faults delimiting areas with different absolute rates. On average the area north of the Baton Rouge fault is subsiding faster than the south, opposite to the long-term sense of fault slip. LiDAR mean vertical rates range between -5 to -11 mm/y and -2.4 to -7 mm/y. InSAR time-series mean rates in the LOS direction range between -10.9 to -13.6 mm/y and -8 to -10.6 mm/y, respectively, for the north and south areas. Subsidence in the northern area likely is controlled by groundwater level changes caused by pumping as indicated by groundwater extraction models. The southern area average is likely influenced by the injection of fluids. Our results suggest volumetric changes caused by fluid extraction and injection in regions separated by growth faults that are creeping to accommodate the spatial variations in subsidence.

Variations in subsidence patterns in the Gulf of Mexico passive margin from Airborne-LiDAR data and Time Series InSAR: Baton Rouge Case Study.

Carolina Hurtado-Pulido[1], Reda Amer[2], Cynthia Ebinger[1], Hayden Holcomb[1]

[1]Department of Earth and Environmental Sciences, Tulane University.

[2]University of Missouri-St Louis, St Louis, Missouri

Corresponding author: Carolina Hurtado-Pulido (dhurtadopulido@tulane.edu)

Key Points:

- LiDAR differencing (1999-2018) and SAR time series (2004-2020) show similar spatial variations. LiDAR documents horizontal changes.
- Subsidence varies between zones separated by growth faults and correlates with groundwater level changes and fluid injection.
- Creep along the Baton Rouge growth fault likely accommodates spatial variations in subsurface fluid levels.

Abstract

The Coast of Louisiana is affected by accelerating sea level rise compounded by land subsidence, leading to land loss. Vertical crustal motions in the region are caused by natural and anthropogenic processes that vary temporally and spatially across the Gulf of Mexico. We investigate the role of growth faulting contributions to subsidence in a case study of Baton Rouge, where two E-W striking, down-to-the-south normal faults, the Denham Springs and Baton Rouge faults, cut compacted Pleistocene strata, and where sediment compaction should be minimal. We used InSAR time series and LiDAR differencing data spanning 1999-2020 to quantify modern vertical and horizontal displacements. After calibration with GNSS data, both methods reveal similar spatial patterns in ground motion, with the faults delimiting areas with different absolute rates. On average the area north of the Baton Rouge fault is subsiding faster than the south, opposite to the long-term sense of fault slip. LiDAR mean vertical rates range between -5 to -11 mm/y and -2.4 to -7 mm/y. InSAR time-series mean rates in the LOS direction range between -10.9 to -13.6 mm/y and -8 to -10.6 mm/y, respectively, for the north and south areas. Subsidence in the northern area likely is controlled by groundwater level changes caused by pumping as indicated by groundwater extraction models. The southern area average is likely influenced by the injection of fluids. Our results suggest volumetric changes caused by fluid extraction and injection in regions separated by growth faults that are creeping to accommodate the spatial variations in subsidence.

Plain Language Summary

Coastal Louisiana is affected by the combination of sea level rise and ground surface sinking, or subsidence. The contribution of subsidence due to natural and human activities varies in time and space. We used airborne LiDAR and SAR satellite data to estimate rates and spatial variations of vertical and horizontal surface motions between 1999 and 2020 in the metropolitan area of Baton Rouge where two faults with surface topography cross the region in a pattern like tilted dominos. We found that the entire area is experiencing subsidence, but that the subsidence rate is faster in the northern fault block than in the southern block of the study area, this pattern is opposite to the long-term fault motion. The spatial pattern of the results from LiDAR and SAR data are similar and relate to groundwater pumping in areas of fast subsidence and wastewater injection zones in areas of slow subsidence. Our results should be considered for future urban planning and water management.

Main Abbreviations

Baton Rouge Fault (BRF); Denham Springs Fault (DSF); Digital elevation model (DEM); Gulf of Mexico (GOM); Interferometric Synthetic Aperture Radar (InSAR); Iterative Closest point (ICP); Light Detection and Ranging (LiDAR); Line of Sight (LOS); Margin of Error (MOE); Persistent Scatter Interferometry (PSI); Relative sea-level (RSL); Root Mean Square Error (RMSE); Sea Level (SL).

1 Introduction

Sea level (SL) rise caused by the combined effects of ice sheet melting and water column expansion owing to increases in ocean temperature will affect at least 190 million people worldwide living mainly in coastal areas (Milliman and Haq, 1996; Kulp and Strauss, 2019;

Frederikse et al., 2020). At regional scales, as in the Gulf of Mexico (GOM), thermal expansion contributes greatly to SL changes (Frederikse et al., 2020). During the 20th century, global SL increased between 12-15 cm (Milliman and Haq, 1996), and it is expected to rise 65 ±12 cm by 2100 (Church et al., 2013; Nerem et al., 2018). The rate of SL rise in the GOM region is accelerating owing to a combination of oceanographic effects (Dangendorf et al., 2023).

Relative sea-level (RSL) is the sum of sea-level rise and vertical crustal motions caused by natural and anthropogenic processes such as fluid extraction, compaction of recent sediments, isostatic adjustments, salt movement, and growth faulting (NASEM, 2018) (Fig. 1). Previous estimates of RSL rate along the Louisiana coast range between 1.38 – 13.2 mm/y; variations between studies depend on methods and local factors (e.g., Penland and Ramsey, 1990; Pendleton et al., 2010; Karegar et al., 2015; Jankowski et al., 2017). Quantifying the different processes using only one method is not an easy task (e.g., Karegar et al., 2020), and all the measurements from different methods should be in the same reference frame (e.g., Shirzaei et al., 2021). Considerable work has been done to quantify rates of sediment compaction in southern Louisiana using Rod Surface Elevation Table horizon markers (e.g., Jankowski et al., 2017; Nienhuis et al., 2017). Quantification of Glacial Isostatic Adjustment (GIA) and anthropogenic contributions lack adequate spatial distribution of GNSS receivers anchored in compacted sedimentary strata across the region (e.g., Dokka 2006; Pendleton et al., 2010; Keogh and Tornqvist, 2019; Karegar et al., 2020). Interferometric Synthetic Aperture Radar (InSAR) offers excellent spatial resolution of vertical crustal movements, and earlier studies in the GOM have detected local and regional variations using individual interferograms and time series (e.g., Jones et al., 2016; Fiaschi and Wdowinski, 2020). Another method consists of using Light Detection and Ranging (LiDAR) data from two different surveys to perform differential LiDAR (e.g., Nissen et al., 2012; Scott et al., 2018; Wheaton et al., 2010). Recently, Zhong et al., (2022) used these two tools in coastal Texas and concluded that the high spatial resolution of LiDAR can improve the results from InSAR time series. InSAR and LiDAR have a good spatial resolution, but the temporal resolution is lower compared to other tools such as GNSS. Integrating all three tools in one area is needed to unravel the causes and spatial variability of vertical crustal movements is critical to mitigation and adaptation programs along the GOM.

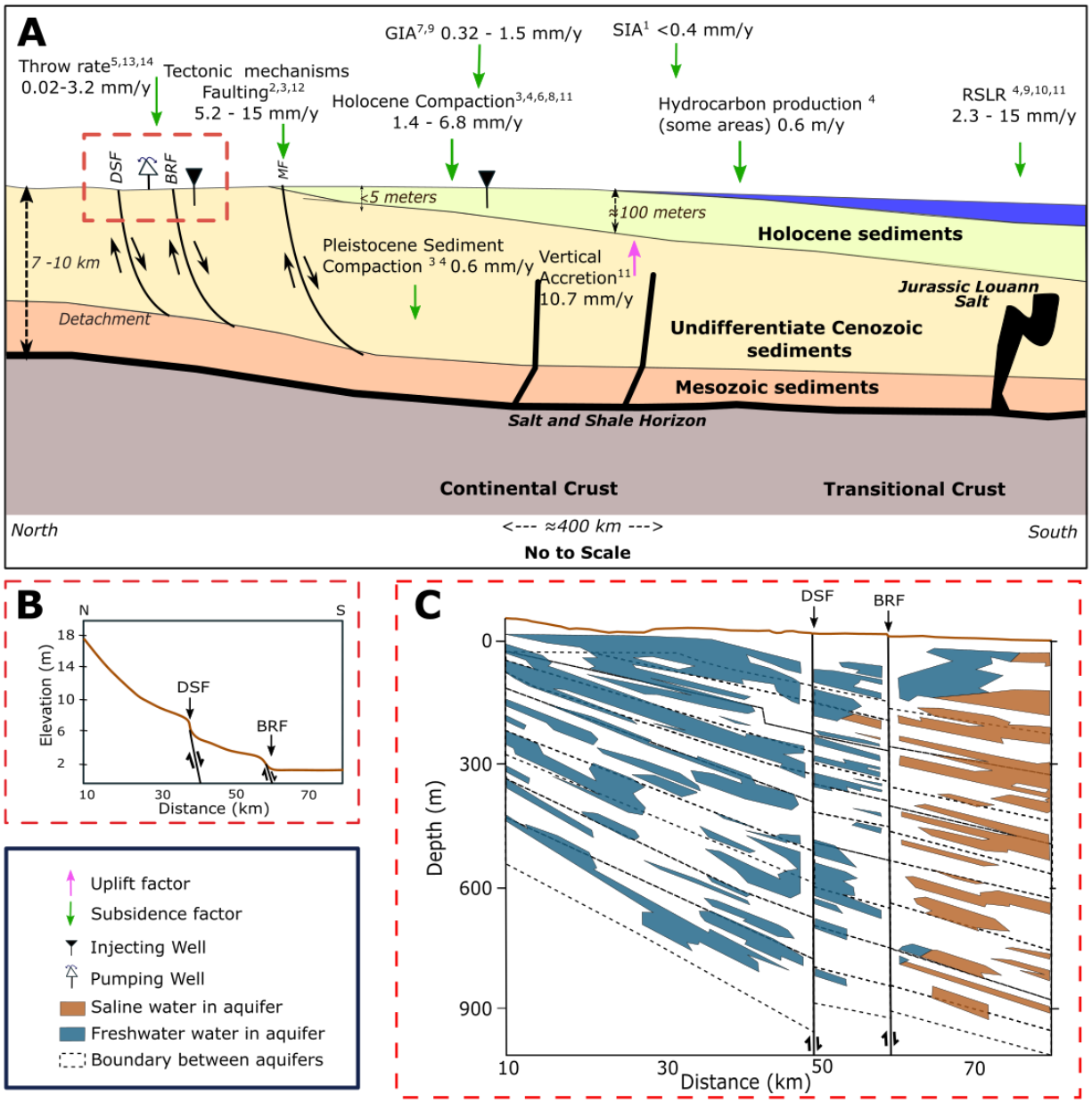

Figure 1: A) Schematic model of the extensional-contractional complex in southern Louisiana. Faults included in the figure: Baton Rouge Fault (BRF), Denham Springs Fault (DSF), Golden Meadow Fault Zone (GMFZ), Michoud Fault (MF). Study area enclosed in red rectangle. Modified from Shen et al. (2017). **B)** Topographic profile of the study area. Modified from Gasparini et al., (2015). **C)** Hydrogeological setting under the study area enclosed in (A). Aquifer boundaries are an approximation for the lithologic, hydrogeologic, and aquifer system contacts. The top one is the 400-ft sand and the bottom one is the 2800-ft (122 m and 853 m respectively) sand, after White (2017). Subsidence and uplift rates from: Kuchar et al. (2018)[1], Dokka et al. (2006)[2], Dokka, (2006)3, Chan et al. (2007)[4], Shen et al. (2017)[5], Keogh and Törnqvist (2019)[6], Love et al. (2016)[7], Karegar et al. (2020)[8], Karegar et al. (2017)[9], Penland and Ramsey (1990)[10], Jankowski et al. (2017)[11], Jones et al. (2016)[12], Penland et al. (2001)[13], Hopkins et al. (2021)[14].

The Baton Rouge region east of the Mississippi River in southern Louisiana is crossed by several E-W striking growth faults that have topographic relief of ~ 5 m, with Quaternary slip rates of < 1 mm/y (Shen et al., 2017)(Figs. 1, 2, 3). Hopkins et al. (2021) measured deformation

of man-made structures of known age in the Baton Rouge-Lake Pontchartrain region to estimate fault slip rates of ~3 mm/y. These rates are 10 times faster than time-averaged rates from Shen et at. (2017) (Fig. 1). The faults cut compacted Pleistocene strata reducing the number of variables contributing to ground subsidence. The study of Hopkins et al. (2021) indicates that fault slip rates are within the range of detection of both LiDAR and InSAR.

Here we use LiDAR and SAR data spanning 1999-2020 to answer the following questions for the Denham Springs Fault (DSF) and the Baton Rouge Faults (BRF) (Figs. 1, 3): 1) Are subsidence rates caused by fault slip significant and measurable using one or both LiDAR and SAR? 2) What areas are affected by fault-controlled subsidence in the Baton Rouge area? 3) Do patterns of vertical crustal movements correlate with fluid extraction and/or urban development? Answering these questions will enable us to verify or refute the following hypotheses: Differencing LiDAR surveys of different periods can detect small vertical motion signal with enough resolution to produce similar results to InSAR; and the BRF and DSF faults are slipping locally due to anthropogenic activities or by natural causes, or a mix of both. *We chose East Baton Rouge as a test study area because there are two growth faults displacing Pleistocene sediments where Holocene sediment compaction is small, enabling us to isolate the signals of fault creep and anthropogenic change (Figs. 1, 2)*. We use information from two continuous GNSS stations processed by the Nevada Geodetic Laboratory (Blewitt et al., 2018) as control points in LiDAR and InSAR data sets. We also compare the results with well data from the Louisiana Department of Natural Resources (SONRIS, n.d.) to investigate whether there is a spatial correlation between fault slip and injection and extraction well volumes and rates over the last two decades.

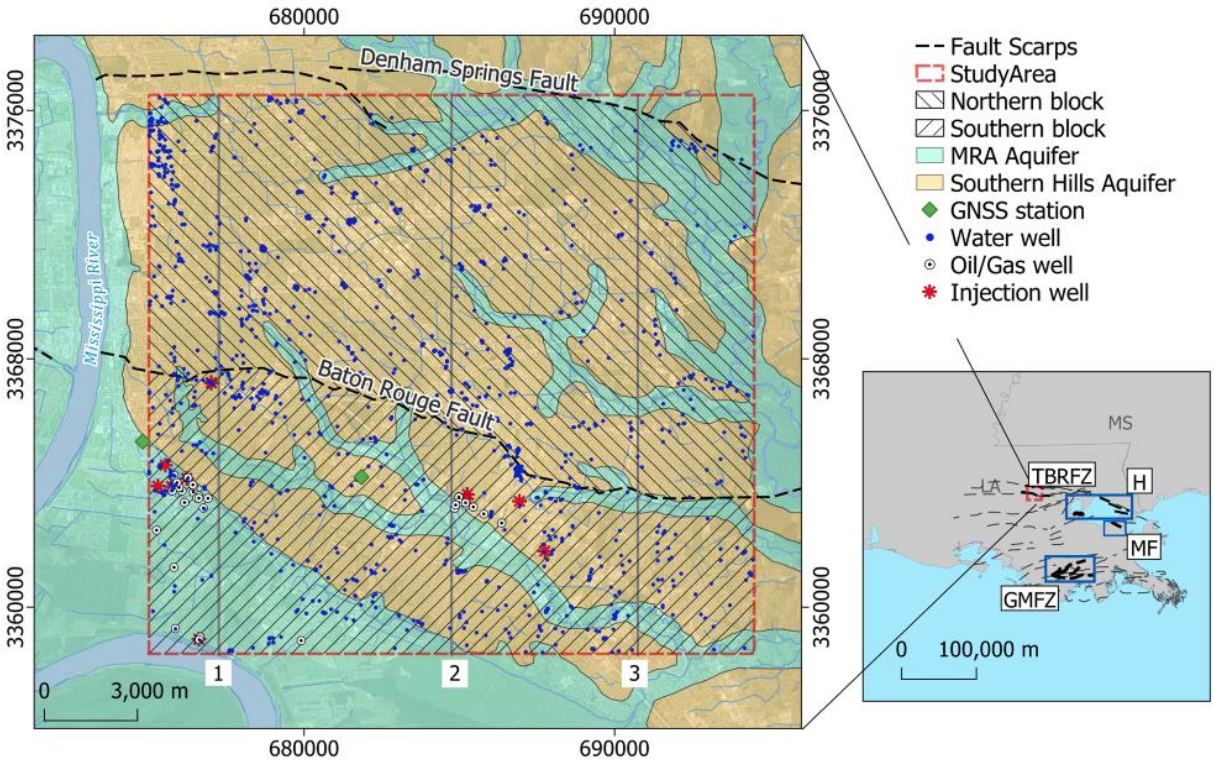

Figure 2: Baton Rouge study area with respect to the Gulf of Mexico margin in Louisiana showing GNSS sites, water and oil/gas extraction wells and injection wells. The Denham Springs (DSF) and Baton Rouge (BRF) are growth faults with Holocene slip (Shen et al., 2017). The Northern block lies between the DSF and BRF; the Southern block is the hanging wall of the BRF. Inset shows the location of the study area with respect to the Mississippi delta, surrounding states, and main fault systems in Louisiana. Michoud fault (MF), Golden Meadow fault zone (GMFZ) and the faults used by Hopkins et al. (2021) (H) are shown. MRA is Mississippi River Alluvial Aquifer. Fault scarps from Culpepper et al. (2019b). Well data and aquifers from the Louisiana Department of Natural Resources (SONRIS), (n.d.). GNSS stations from the National Geodetic Survey (n.d.). Gray vertical lines and numbers are profiles for Figure S1. Base map imagery from QuickMapServices - QGIS (Map data ©2015 Google).

1.1 Background

The GOM is a passive margin that formed between 200-158 Ma during the breakup of Pangea, resulting in pervasive, general E-W-striking normal fault systems bounding 3-10 km-deep sedimentary basins (e.g., Sawyer et al., 1991; Pindell and Kennan, 2009; Eddy et al., 2014). Mesozoic growth faults in the Mississippi delta are listric faults that detach on salt horizons (Durham and Peeples, 1956; Culpepper et al., 2019). These faults accommodated extension until ~40 Ma, but much slower movement associated with compaction and salt migration has continued to present day (Shen et al., 2017). Despite the ~5 m fault scarps (Fig. 3) and evidence for ongoing movement, there are only three instrumentally recorded earthquakes of M2.4-3.8 along the coastal fault systems of Louisiana (Stevenson and Agnew, 1988; Walter et al., 2016), suggesting that slip occurs primarily by creep.

The GOM is characterized by its low elevation coasts, broad continental shelf, steep continental slope, and a basin as deep as 4400 meters (e.g., Turner and Rabalais, 2018). The Mississippi River flows into the GOM, through the Mississippi delta. The delta began to develop at ~100 Ma with the formation of the Mississippi embayment, which concentrated sediment input to the gulf. During the last 7000 years, the delta depocenter relocated at least six times in response to climate and sea-level changes (Blum and Roberts, 2012). In the last 100 years, the Mississippi delta has suffered drastic land loss (Gagliano et al., 1981). This could lead to a shift of the depocenter of the Mississippi delta caused by sea-level rise, climate change, anthropogenic activities, and the lack of sediment delivery caused by artificial dams (e.g., Blum and Roberts, 2012). Glacial Isostatic Adjustment (GIA) and Sediment Isostatic Adjustment (SIA) contribute to long-term subsidence (e.g., Kuchar et al., 2018). GIA was modeled using RSL data from tide gauges and vertical and horizontal velocities from GNSS between 2006-2015 along the GOM by Love et al. (2016). During this century GIA in southeast Louisiana will contribute approximately 30 mm to RSL rise with a rate of 0.32 mm/y (Love et al., 2016). On the other hand, SIA registers a rate of less than 0.5 mm/y on areas with thicker Holocene sediments (Wolstencroft et al., 2014; Kuchar et al., 2018).

Holocene sediment thickness increases following the shape of the Mississippi river, reaching a thickness of 100 meters at the shoreline (Penland and Ramsey, 1990). Compaction and compression of Holocene sediments are the primary factors causing subsidence on the Mississippi delta in areas close to the shoreline (e.g., Penland and Ramsey, 1990; Karegar et al., 2015; Karegar et al., 2020). Shallow subsidence in the uppermost 5 meters in the Mississippi delta accounts for more than 60% of the total subsidence in the coastal area with rates varying between 6.4±5.4 and 9±1 mm/y (Keogh and Törnqvist, 2019; Jankowski et al., 2017; Nienhuis et al., 2017).

Despite the importance to infrastructure, there are just a few studies that have quantified fault slip rates and their relationship with subsidence at different time scales in the area, with rates ranging between 0.02 – 16.9 mm/y (Gagliano et al., 2003a, 2003b; Dokka et al., 2006; Shen et al., 2017; Culpepper et al., 2019a; Hopkins et al., 2021). Fault slip and creep are difficult to quantify because they can be episodic and slow, and the signal can be masked by faster processes such as sedimentation (Gagliano et al., 2003b). Salt movement may reactivate some fault segments (Gagliano et al., 2003a). Local subsidence has been related to the presence of fault

traces and fluid extraction sites (e.g., Kuecher et al, 2001; Morton et al, 2002; Dokka, 2011). Dokka (2006) and Dokka et al., (2006) interpreted episodes of subsidence along the Michoud fault (MF) between 1955 to 2005 as evidence of episodic fault slip, although they could also be caused by groundwater extraction (Jones et al., 2016). Fault motion and subsidence near the Golden Meadow fault zone (GMFZ) have been related to hydrocarbon extraction (e.g., Morton et al., 2002; Chan and Zoback, 2007).

There is visual evidence of building and road displacements along the BRF and other coastal faults with measured rate estimates of ~3 mm/y (McCulloh, 2001; Hopkins et al., 2021). The BRF and DSF reactivated during the Pleistocene due to depositional loading (McCulloh and Heinrich, 2013). Shen et al. (2017) calculated mean fault throw rates in the eastern portion of the BRF using optically stimulated luminescence dating. Their results indicate that the faults have an average slip of 0.22 mm/y for the past 4,000 years and between 0.02-0.07 mm/y for the last 130,000 years for areas lying on Pleistocene sites. The relief caused by Pleistocene-Recent slip along the BRF is clear in DEMs produced from LiDAR data (Fig. 3). Faults in this system merge at a depth of ~6 kilometers into a detachment that sits on an overpressured layer of salt and shale that dips with an angle between 45° to 65° (Gagliano et al., 2003a; Shen et al., 2017) (e.g., Figs. 1).

Local subsidence has been related to the presence of fault traces and fluid extraction sites (e.g., Kuecher et al, 2001; Morton et al, 2002; Dokka, 2011). Wells in Baton Rouge have multiple purposes like water, gas and oil withdrawal, water injection and monitoring, with depths ranging between 4-6000 meters. The change of pore fluid pressure underground caused by fluid extraction/injection changes the volume at depth, which could influence fault activation (e.g., Kuecher et al., 2001). Multiple studies have related extraction of fluids with local subsidence at different locations (e.g., Jones et al., 2016; Puskas et al., 2017; Li et al., 2020), and uplift with injection of fluids (Teatini et al., 2011; Shirzaei et al., 2016).

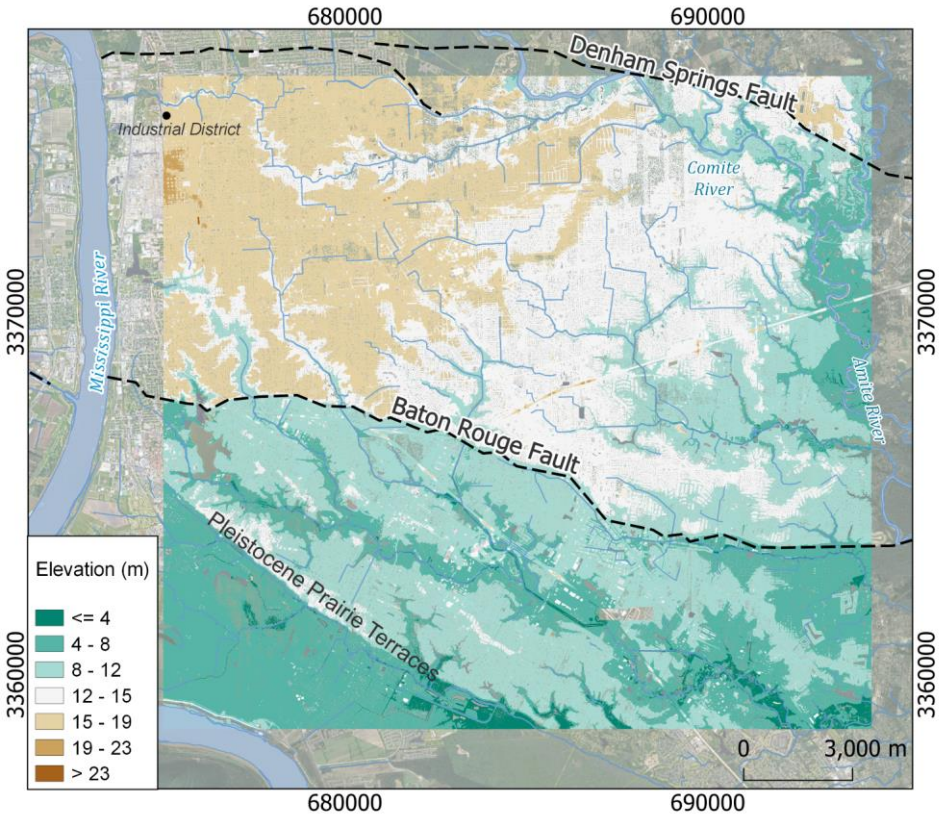

Figure 3: Digital Elevation Model from the study area showing the topographic relief across the Denham Springs and East Baton Rouge faults (dashed lines). The geological contact labeled as Pleistocene Prairie Terraces marks the edge of the natural levee in the area. We created this DEM using LiDAR point cloud from the 2018 survey. Base map imagery from QuickMapServices - QGIS (Map data ©2015 Google).

The aquifer system in Baton Rouge is part of the Southern Hills aquifer and the Mississippi River Alluvial aquifer (Tomaszewski et al., 2002) (Fig. 2). The former is composed of interbedded layers of compressed clay/silt and layers of porous sands (Fig. 1). The sands south of the BRF are more continuous than those north of the fault (Vahdat-Aboueshagh and Tsai, 2021). These sands form ten independent aquifers named after their depth under the Baton Rouge industrial district, with depths between 122 to 823m (400 ft to 2700-ft) (Tomaszewski et al., 2002). Large volumes of groundwater removal have affected reservoirs in the Baton Rouge area forming cones of depression at local and regional scales (White, 2017; Chen et al., 2023), and saline water from southern areas has intruded into some of these sands (Nasreen, 2003; Elshall et al., 2013). Similarly, other areas in Louisiana have shown saline intrusion in areas of fault motion (e.g., Kuecher et al., 2001). Deep aquifers have larger withdrawal volumes, and, therefore, have been more affected during the last decades (Tomaszewski et al., 2002; Nasreen, 2003). The Mississippi River Alluvial aquifer has not had a significant groundwater level

decrease, and saline water has not infiltrated the eastern portion of the aquifer where the study area is located (Tomaszewski et al., 2002; Nasreen, 2003; Chen et al., 2023).

The BRF plays an important role in the dynamics of the aquifers in Baton Rouge; it is a barrier for saline water coming from the southern area, but it may serve as a conduit and can allow lateral intrusions due to pumping of groundwater at the north of the fault (Nasreen, 2003; Elshall et al., 2013; Anderson et al., 2013; Chen et al., 2023). The DSF is permeable and allows freshwater to flow down to the south, where pressure gradients cause southward flow and recharge to the aquifers in the area between the two faults (Elshall et al., 2013).

2 Data

2.1 SAR data

SAR datasets were acquired by the EnviSAT and Sentinel-1 satellites. Both acquire data on the C-band (5.405 cm) and produce Single-Look Complex images. We used vertical transmit and receive polarization (VV). The EnviSAT dataset was collected between 2004 and 2010 in the relative orbit 83 and it is composed of 18 scenes (ESA, 2021a) in descending mode. The Sentinel-1 dataset was collected in Interferometric Wide mode between 2017 and 2020 and consists of 33 scenes all acquired in the relative orbit 165 (ESA, 2021b) in ascending mode. Each of these datasets forms a different time series that was analyzed separately. The list and dates of images is in Table S1.

2.2 LiDAR data

LiDAR point clouds come from two surveys that cover the portion of the BRF and DSF, East Baton Rouge parish. The first dataset was collected in March of 1999, has a point space of 4 m (0.0625 points/m^2), a pulse rate of 15 kHz and a vertical accuracy measured as the Root Mean Square Error (RMSE) of 15 cm (USACE, 2001). The newest was collected between March and April of 2018, has a point space of 0.33 m (9.2 points/m^2), a pulse rate of 450 kHz and a vertical accuracy of RMSE=3.6 cm (USGS, 2019). For more details see Table S2.

2.3 Well data

Data about injection and extraction of fluids from the wells comes from the Louisiana Department of Natural Resources website. The wells included here are those that were active between 1999 and 2020 or for a shorter time in that period and were in the database by August

2021. For wells extracting water, we only used active wells whose main function was water pumping. In the case of wells producing oil and gas, we only considered those with gas production of at least 200,000 MCF or produced more than 20,000 m^3 of oil during the study period (Fig. S4). Not all the wells have complete information about volume of production or injection, but if they appeared as active, we included those for location information in our maps. Table 1 summarizes the number of wells found and used. However, wells that were operating before can, in some cases, caused delayed pore pressure changes and deform the surface (Shirzaei et al., 2016).

Table 1: Number of wells in the study area per fluid. This table excludes 1908 wells that are used to monitor water level and quality.

	Water	**Oil – gas**	**Injection**
Total wells in area	821	368	24
Current active wells (By august/2021)	470	6	2
Active wells between 1999 -2021	592	47	13
Wells with volume extraction/ injection information		23	9

2.4 GNSS time series

There are two continuous GNSS stations in the study area (Fig. 2). Both stations are mounted on buildings and there is no public information about the foundation depth for any of the stations. The 1LSU station worked between 2004-2022 and it is mounted on the Patrick F. Taylor Hall building, constructed on the Mississippi River Alluvial Aquifer (Fig. 2) and the Pleistocene Terraces (Fig. 3). The local geology makes the 1LSU site sensitive to hydrological changes of the Mississippi River as compared to the SJB1 station. The SJB1 station has acquired data between 2009-2023 and it is mounted on the LifeShare Blood Center constructed above the Southern Hills aquifer which lies at deeper depths than the Mississippi River Alluvial Aquifer and does not have direct contact with any water body (Fig. 2). North, east, and up velocities of the GNSS stations are calculated by the Nevada Geodetic Laboratory (Blewitt et al., 2018). Vertical time series for both stations are in Fig. S3.

3 Methods

3.1 Persistent Scatter Interferometry - PSI (time series InSAR)

PSI is a differential InSAR technique that allows one to use the phase information from multiple SAR images acquired at different times to estimate phase changes between several interferograms. Phase change information is used to calculate the velocity of displacement and the displacement time-series during the study period (Hooper et al., 2004; Crosetto et al., 2016). PSI uses pixels with low phase noise, called Persistent Scatterers (PS), across lengthy time intervals in multi-temporal data. It is particularly useful in urban areas that have a high density of persistent, or permanent, scatterers (Ferretti et al. 2001; Crosetto et al., 2016). Displacement is calculated on the Line of Sight (LOS), projecting 3D displacements into 1D displacements in the LOS direction (Crosetto et al., 2016). One of the advantages of this technique is its ability to detect signals of ground displacement at millimetric scales with an accuracy of millimeters depending on the number of images in the time series, the density of PS, temporal baseline dispersion, and terrain conditions (Ferretti et al., 2001; 2004; 2007).

A description of this technique is found in the official manuals (L3Harris, 2014; 2021), Ferretti et al., 2001, and in the Supplemental material (T1). We used SARscape software (version 5.6; 2021) to calculate vertical displacement velocity for both datasets. The topographic phase was removed using the Shuttle Radar Topography Mission DEM. Orbital errors can be ~0.5 mm/y/100 km for EnviSAT and ~0.2mm/y/100 km for Sentinel-1 in the LOS direction (Fattahi and Amelung, 2014), but effectively cancel for InSAR time series with several images as the ones presented here. Ionospheric errors are negligible because we are using data captured on the C-band and the study area is at midlatitude where ionospheric corrections are not recommended (Liang et al., 2019). Tropospheric phases are estimated from the residuals from the linear model calculated by SARscape (Ferretti et al., 2001; Supplemental material - T1). To provide a numerical approximation of the tropospheric variation over the study area during the study period we present an empirical analysis using GACOS data (Yu, et al. 2017; Supplemental material – T2). For the EnviSAT time series (2004-2010) the average range of the tropospheric delay is 28.75 mm and for Sentinel-1 time series (2017-2020) it is 35.95 mm.

We multilooked the data to reduce decorrelation noise and build the spatial coherence map (Goldstein et al., 1988; Fig. S5). For the EnviSAT dataset we used four azimuth-looks and one range-look; for the Sentinel-1 dataset we used five azimuth-looks and one range-look. The

entire area is divided into sub-areas, each is 25 km^2 and every subarea is independently processed. By default, just one reference point is selected for each subarea. Reference points were selected using an Amplitude Dispersion Index >60%. A 30% overlap of subareas is used in the mosaicking process to merge all the sub-area results. The merging process is carried out considering a Super Reference Point (Fig. 4 and 5) which is characterized by the highest Amplitude Dispersion Index among the others. Coherence used for merging all sub-areas is 0.77.

3.2 LiDAR pre co-registration

Co-registration of the LiDAR point clouds is the process of aligning datasets acquired at different times over the same area. It is important to know the magnitude and the direction of the horizontal misalignment to correct the geographical location of the point clouds to improve vertical differencing between corresponding points. This process reduces systematic errors (Anderson, 2019). Misalignments between the point clouds can be caused by 1) distortion of the point clouds from measurement errors related to flight discrepancies; 2) real changes in the landscape (subsidence, uplift, translation, vegetation growth, mass movement); and 3) local topographic relief on flat surfaces where there is less random LiDAR scattering (Scott et al., 2018).

We conducted point cloud co-registration using ICP (Section 3.3) in two ways: using only LiDAR ground points and using LiDAR points from structures that should be stable over time and are anchored to some foundation depth (e.g., Fig. S2). For the first approach, ground points were taken using the original classification of both point clouds done by the distributors. For the second approach, a feature-based technique allows us to take information from structures that are expected to be stable and use them as control points (Brook and Ben-Dor, 2011). Using Point Data Abstraction Library (2018) filters (PDAL), we created a new point cloud for each dataset whose points only belong to structures that satisfy specific criteria. First, the point must be on a plane. To evaluate this criterion, we used the filter “estimaterank”, which categorizes each LiDAR point in a line, plane, or a 3D structure. Secondly, the points must be in an elevation range assigned depending on if they are in the hanging wall or footwall of the BRF. The range for the hanging wall is 7 m to 35 m and for the footwall is 12 m to 35 m. These values were chosen from observation of the LiDAR data, using the maximum value from tall buildings and the lowest from roads and parking lots. DEMs show that there are at least ~5 m of relief along the BRF (Fig. 3); therefore, features on the hanging wall are expected to be at a lower elevation.

We allowed for North and East movements of the 2018 (newest) point clound to co-register the 1999- and 2018-point clouds. The translation amount was estimated by ICP. We calculated the average motion in the east and north components for areas of 2.25 km^2. This process ensures that vertical DEM differencing is more accurate. We did this process with ground LiDAR points and LiDAR points from stable structures.

3.3 Iterative Closest point – ICP

This algorithm allows one to perform 3D LiDAR differencing by calculating rotations and translations of a surface (Scott et al., 2018; Nissen et. al., 2012). The ICP algorithm aligns the point clouds using user-defined core points in the two datasets. Each core point is defined by a grid of 50 m and centered in a square or window of 50x50 m in the 1999-point cloud and 51x51 m in the 2018-point cloud. We chose these values for computational optimization. The horizontal coordinates of each core are the central point in each window. ICP assumes that each window behaves as a rigid body (Nissen et. al., 2012).

This algorithm iterates as follows for each window: 1) Find the closest point in the old point cloud for each point in the new point cloud, 2) Calculate translation and rotation of each point in the old point cloud, 3) Iterate until a minimum distance is reached or until a certain number of iterations are completed (Scott et al., 2018; Nissen et. al., 2012). We iterated until the translation was less than 10^{-4} meters or when 10 iterations were completed. ICP applies a linear transformation to the old data to have the best alignment possible. It finds the rigid body transformation matrix, with α, β and γ representing the rotations on the x, y, and z axes, and $\boldsymbol{t_x}$, $\boldsymbol{t_y}$, $\boldsymbol{t_z}$ representing the translations in the same three axes in equation 1 (Scott et al., 2018).

$$\boldsymbol{PC_{new}} \approx \boldsymbol{PC_{old\ transformed}} = \begin{pmatrix} \mathbf{1} & -\boldsymbol{\gamma} & \boldsymbol{\beta} & \boldsymbol{t_x} \\ \boldsymbol{\gamma} & \mathbf{1} & -\boldsymbol{\alpha} & \boldsymbol{t_y} \\ -\boldsymbol{\beta} & \boldsymbol{\alpha} & \mathbf{1} & \boldsymbol{t_z} \\ \mathbf{0} & \mathbf{0} & \mathbf{0} & \mathbf{1} \end{pmatrix} \boldsymbol{PC_{old}} \qquad (\boldsymbol{Eq.1})$$

Where $\boldsymbol{PC_{new}}$ is the newest LiDAR point cloud, in this case the one from 2018, $\boldsymbol{PC_{old}}$ is the original and oldest LiDAR point cloud, here corresponding to the one from 1999, and $\boldsymbol{PC_{old\ transformed}}$ is the transformed old LiDAR point cloud. We run the ICP algorithm with LiDAR ground points and with LiDAR points from stable surfaces chosen in the co-registration section. In both cases, ~122,400 core points and windows were created. The windows do not have the same number of LiDAR points. The results of this ICP implementation provide the amount of

translation that must be applied to each window in the newest point cloud to align the dataset with the oldest point cloud. The translations of each window are represented on each core point.

These results were filtered to have only displacements between 0 to 1 m to eliminate outliers (e.g., new constructions), and not natural displacements. Then, results were averaged to have a representative point per 2.25 km^2. The error for this process is given initially by the Point-to-Plane error metric (Scott et al., 2018; Nissen et. al., 2012), and the final averaged results were evaluated using a 95% margin of error and the residual systematic error described on section 3.5. We use the 3D_Differencing MATLAB code created by Scott et al. (2020) to apply ICP to LiDAR data, which uses the LIBICP (LIBrary for Iterative Closest Point fitting) software created by Geiger et al. (2012) to solve the rigid body transformation. The horizontal translations calculated by ICP are used to co-register the datasets (Section 3.2), but these displacements can include real motion. We discuss the real part of this motion in the results and discussion sections.

3.4 Vertical DEM differencing

Vertical differencing between the two data sets is achieved using Geomorphic Change Detection (GCD) software. It allows one to detect topographic and volumetric changes using digital elevation models (DEM) (Wheaton et al., 2010). With GCD we created a DEM of Differences doing pixel by pixel differentiation. The vertical accuracy of these is given by standard error propagation and depends on the accuracy of the original point clouds (Wheaton, 2018). We created the DEMs using PDAL filters to include only co-registered ground LiDAR points. We used Inverse Distance Weighting with PDAL tools to interpolate the data (Shepard, 1968). We used a pixel size of 5 m, and a radius of 5 m for the 1999-point cloud and 3 m for the 2018-point cloud. The radius is different to ensure that the DEMs from 1999 have enough points to interpolate. We used a power parameter equal to 2 because it has been shown to produce good empirical results and it is computationally efficient (Shepard, 1968). The error of each DEM with respect to the original LiDAR data was estimated using the root mean square error metric. Figure S10 shows the workflow followed to process the LiDAR data.

3.5. Error estimation

Systematic errors can impact the estimated changes from LiDAR. As we co-registered the data, it is expected that systematic errors caused by flight discrepancies are reduced but not completely removed (e.g., Anderson, 2019). This error type can dominate the error budget in the

analysis of vertical ground changes (e.g., Anderson, 2019). We assume a residual systematic error from the LiDAR results (Fig. 7A and 7B) of 44.8 mm (2.3 mm/y). This number is the difference between the results of ground and stable surfaces on the fourth row from Figure 7A and 7B where ab E-W stripe appears. The systematic problems are probably E-W flight line errors.

We present uncorrelated random errors as the Margin of error (MOE) of the Mean. It is calculated as $\boldsymbol{MOE_m = z \times \frac{\sigma}{\sqrt{n}}}$. Where $\boldsymbol{z}$ =1.96 corresponds to a confidence level of 95% for the average mean, $\boldsymbol{\sigma}$ is the sample standard deviation of the mean averaged points, and *n* the sample size. We used this metric to quantify the random component of the error due to the different areas for each sampling (2.25 km^2 and for each block of the fault ~175 km^2), but not for individual points. The total uncertainties should include the RSE to better bound the results. In the case of LiDAR, we are aware that each survey has an associated RMSE estimated by the distributor (Section 2.2). The RMSE quantifies the discrepancy between the location of checkpoints and the Triangulated Irregular Network generated from the point clouds by the distributors (USACE, 2001; USGS, 2019). Then, in the worst case, each pixel on each DEM can be wrong by 15 cm and 3.6 cm in the vertical component, if each pixel in each DEM only contains one LiDAR point from each survey, and the vertical change in each pixel could have an error of 15.43 cm. This extreme case is not a concern owing to our approach of comparing areas from each survey and not individual pixels. For instance, each ICP - LiDAR window of 50 m may have ~100 LiDAR points in each point cloud. Using the results of displacement for each window (Section 3.3) we found the mean vertical displacement for 2.25 km^2 areas, then we calculated the corresponding MOE with the number of windows (~1000) as the sample size. For InSAR time series we present MOE using the total number of PS points for each block as the sample size. Systematic errors for InSAR time series were corrected during the PSI processing and their ranges are described (Section 3.1 and Supplemental material – T1).

3.6. Tie of Results

We used the 1LSU station as a tie point for all the results but EnviSAT and SJB1 as a control point to compare the results after this connection. We selected 1LSU because has the longest time series between the two stations. The results from the three geodetic tools (GNSS, InSAR time series, and LiDAR differencing) are in different reference frames, so we

transformed the GNSS velocities (with plate fixed) from ITRF2014 to NAD83 using the online application Horizontal Time-Dependent Positioning from NOAA (Pearson and Snay, 2013).

To tie the results, we calculated the difference between the displacement of 1LSU and the results from LiDAR and InSAR time series in the location of the station. Then, that difference is added/subtracted from each dataset to match the results with the results of the 1LSU station in that location, such that all the results are referred to the same point (Mahatra et al., 2018). The InSAR time series were tied to 1LSU by projecting to the LOS displacements of the station using the incidence and heading angle for each dataset. For ICP, the tie with 1LSU was done in the three components, and for LiDAR differencing it was done only in the vertical component. Due to this process, the original results are moved by a constant, and this process does not change the errors.

4 Results

4.1 Velocities from InSAR time series – Envisat and Sentinel-1

The results of the InSAR time series created with Sentinel-1 data do not show results for the footwall of the DSF (Fig. 4) and the results from EnviSAT are very noisy to interpret (Fig. 5). The area covered by our study area at the north of the DSF is mostly covered by vegetation, so there is high decorrelation and there are not enough persistent scatterers (Fig. 4B). We therefore focus on the BRF.

For the case of discussion, we call the footwall block of the BRF the northern block and the hanging wall of the BRF the southern block as indicated in Figure 2. After removing the difference of motion with the GNSS station 1LSU from the results, the InSAR time series using Sentinel-1 indicates that the northern block is moving away from the satellite at a larger rate than the southern block (Fig. 4A). PSI detected 411,857 persistent scatterers. Areas labeled as Agricultural, or Park/Water (Fig. 4B) do not have enough persistent scatterers. Therefore, we cannot produce results over these areas with PSI. The mean velocity between 2017-2020 using Sentinel-1 data for the complete northern block is -13.65±0.00471 mm/y while the southern block has a mean velocity of -10.559±0.00895 mm/y. The SJB1 station differs from the InSAR time series in ~2.33 mm/y (Fig. 4).

Figure 4C shows some examples of the time series in the area. Each time series is the average displacement of the persistent scatterers that are in a specific location (details in Table

S3). The time series of P6 shows less displacement; it is located on the Baton Rouge Wastewater Treatment plant which lies ~500 m from injection well 200837 and ~2000 m from the 136676 injection well. The time series for the building where the SJB1 station is anchored and the area P5, which surrounds the injection well 189576, are the next series with less displacement. The areas identified as P2, P3, and P4 have similar displacements and are the sites closest to the BRF.

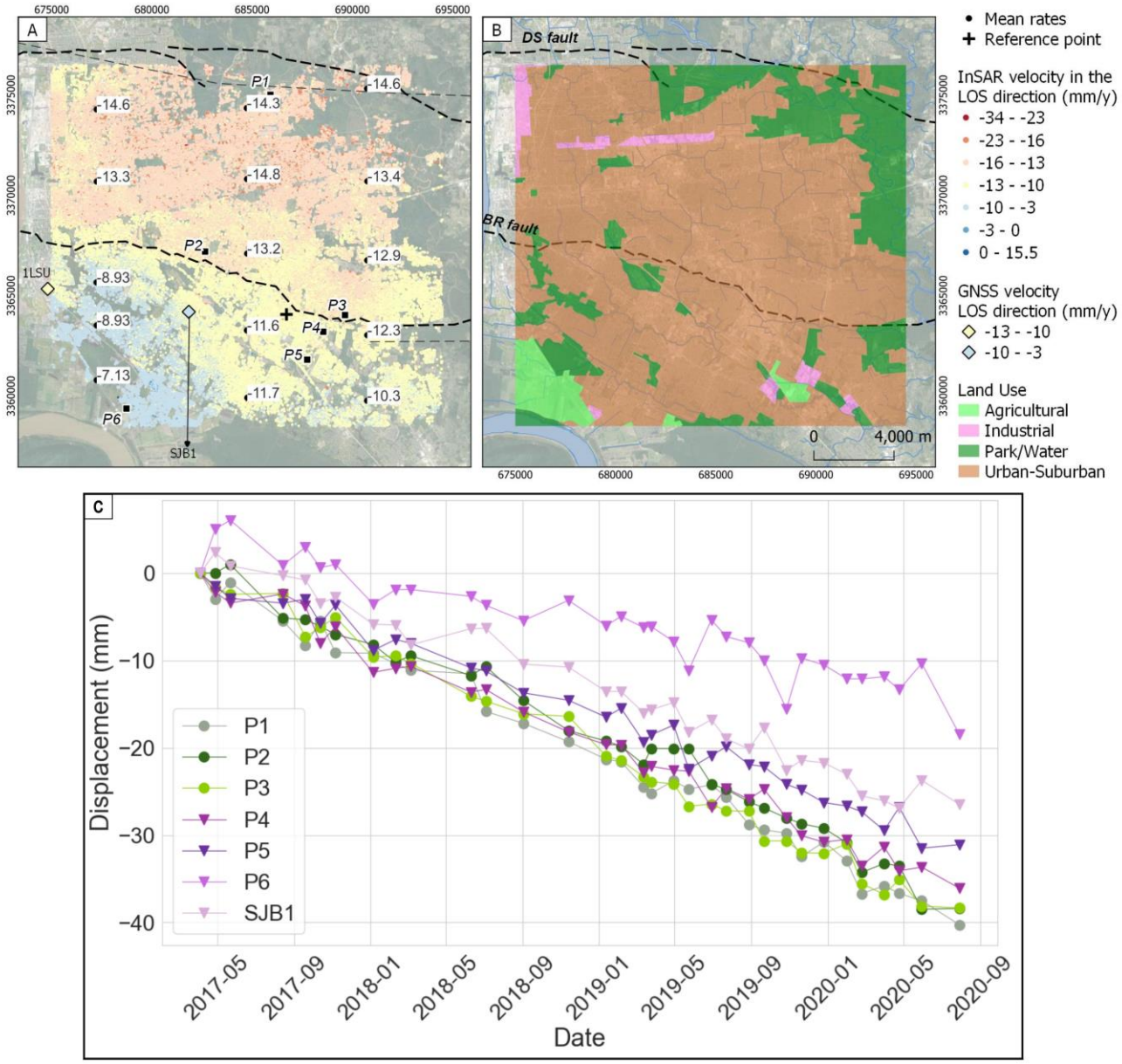

Figure 4: Rates produced with Sentinel-1 (2017-2020) compared to Land use. **(A)** Displacement rates in the LOS direction calculated with the PSI method. These results are tied to the 1LSU GNSS station. Numeric labels in the image indicate mean rates for the black dots. The cross is the initial reference point used to create the time series.

Rhombuses are the average velocities of the GNSS CORS stations in the LOS direction on the Sentinel-1 geometry (ILSU -10.88 mm/y and SJB1 -8.404 mm/y). **(B)** We mapped land use using the basemap imagery from QuickMapServices - QGIS (Map data ©2015 Google) at a scale of 1:10.000. **(C)** Time series examples located in (A); green colors show samples in the northern block and purple colors show samples in the southern block. These time series are the average of the displacements of the points that landed in the same construction, with details on Table S3. Displacement in the LOS direction.

The velocity in the LOS direction for the study area using EnviSAT data is shown in Figure 5A. This dataset does not cover the 1LSU station, and it is the only one that was tied to the SJB1 station. The PSI process detected 172,791 persistent scatterers. These results are noisy in some areas, although it is possible to see similar patterns with the results of Sentinel-1 analyses. Figure 5A shows that the entire area is subsiding but the northern block is moving away from the satellite faster than the southern block. The northern block is moving with a velocity of -10.869±0.0384 mm/y and the southern block at a rate of -8.030±0.0614 mm/y. The noise also can be related to land-use changes during that period after Hurricane Katrina in 2005. This will be further explained in the discussion section.

The example time series with EnviSAT shows that the P3 area was the most stable among these examples, although it is close to the reference point of the time series in this dataset. Sample P3 shows a large mismatch between the Sentinel-1 and EnviSAT results (Fig. 4C and 5B), but this area has homes constructed in 2017, before the area showed fewer coherent persistent scatterers in EnviSAT as compared to Sentinel-1 data. We suspect that the change in land use contributes to differences between datasets. The other areas show a similar behavior (Fig. 5B). Details about each time series are in Table S3.

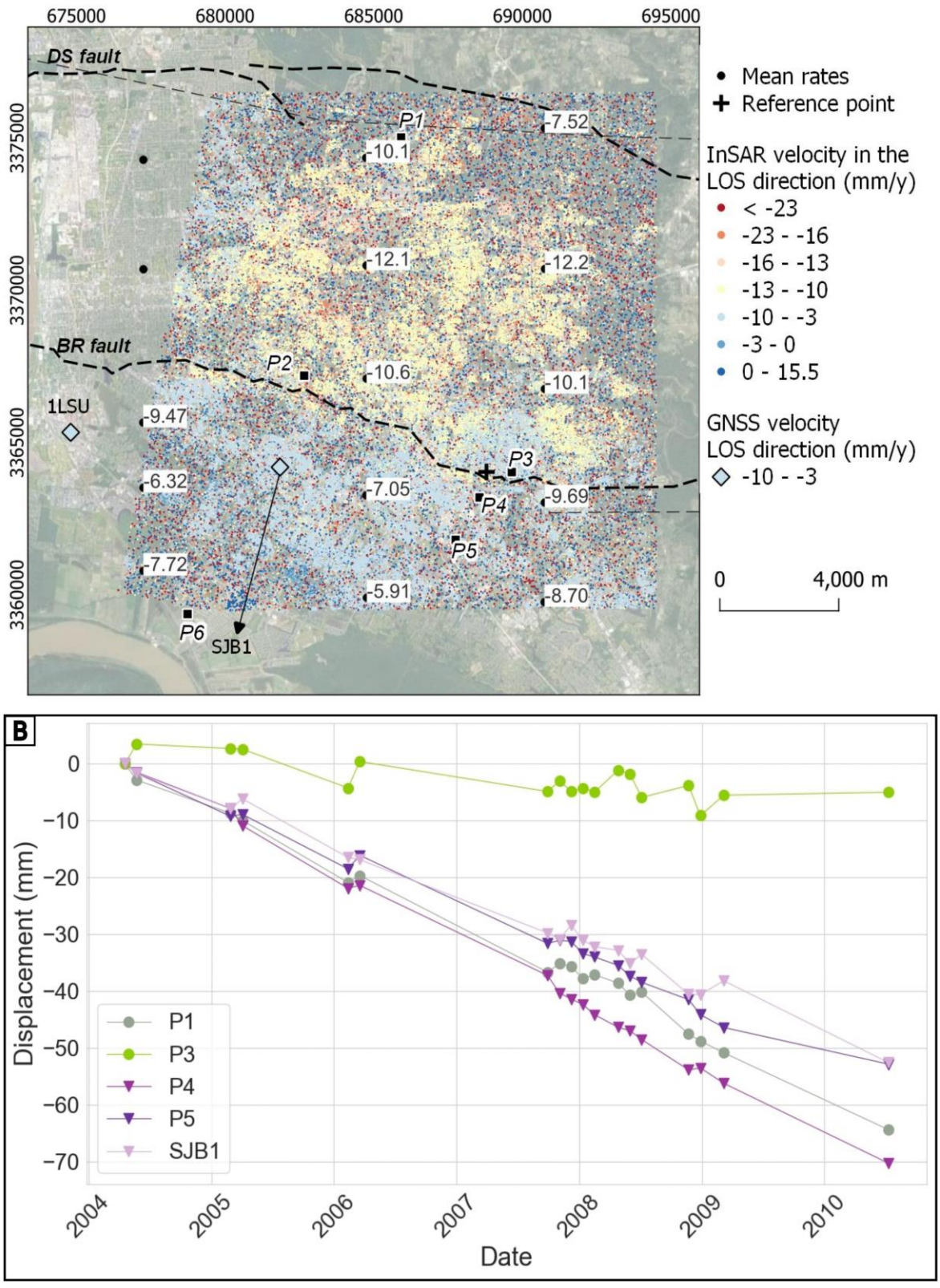

Figure 5: Rates produced with Envisat data (2004-2010) **(A)** Displacement rates in the LOS direction produced using the PSI method. These results are tied to the SBJ1 GNSS station. Numeric labels in the image indicate mean rates for the black dots. The cross is the reference point used to create the time series. Rhombuses are the average

velocities of the GNSS CORS stations in the LOS direction on the EnviSAT geometry (ILSU -9.81 mm/y and SJB1 -7.23 mm/y). **(B)** Time series examples located in (A); green colors show samples in the northern block and purple colors show samples in the southern block. These time series are the average of the displacements of the points that landed in the same construction, with0020details on Table S3**.** P2 and P6 do not have a time series because the construction was not in place before 2010. Displacement in the LOS direction. Base map imagery from QuickMapServices - QGIS (Map data ©2015 Google).

4.2 LiDAR Horizontal displacement from ICP

The results from ICP indicate that overall, the entire area moved towards the east direction between 1999-2018 in the NAD83 reference frame (Fig. 6). Results of horizontal displacement created with two different LiDAR classifications – ground LiDAR points and stable surface LiDAR points (Fig. 6B) – have different spatial behaviors in some areas. Horizontal displacements estimated using just ground LiDAR points (Fig. 6A) are more homogenous showing that the whole area moved to the east with small displacements in the north component (Table 2).

The horizontal displacement calculated using LiDAR points on stable surfaces shows more heterogenous behavior (Fig. 6B). In the north area of the northern block most areas moved to the east direction, but in the southeast of the same block near the BRF, the direction is mostly north-east (Table 2). These results also show that the largest errors occur in the areas closer to the eastern section of the BRF. A caveat of only using LiDAR points on stable surfaces is that this set of points is less dense than the set of ground points, and affected mostly by the oldest LiDAR survey, which may explain why the errors are smaller in the case of only ground LiDAR points.

Our results agree in the direction of motion with the motion of the SJB1 station (Fig. 6, Table 2). The magnitude of the motion using the rates from the GNSS SJB1 station between 1999-2018 is 42.18 mm to the north and 260.11 mm to the east. Comparison to the results with LiDAR ground points (Fig. 6A), shows almost double our estimate in the north component but a difference of only 3 mm in the east component, considering the mean value of the block. Comparison of SJB1 GNSS station with the results with only LiDAR points on stable surfaces (Fig. 6B) shows that the north component is smaller by ~13 mm and larger in the east component by ~35 mm.

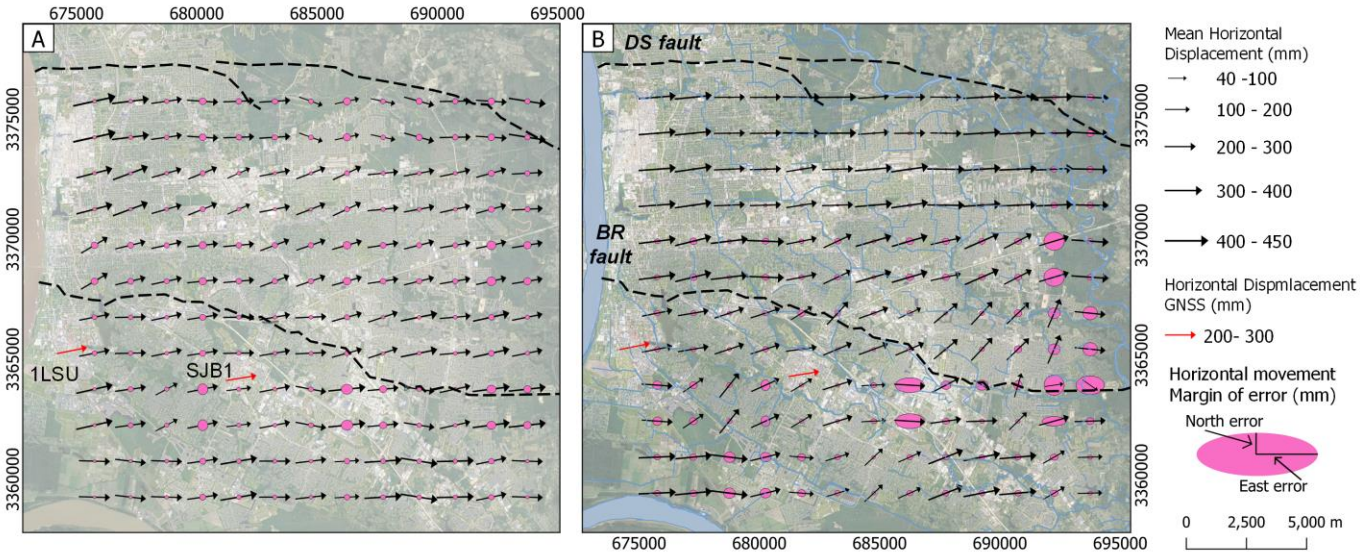

Figure 6: Horizontal displacements calculated with the ICP algorithm. **(A)** Horizontal displacements using ground LiDAR points. **(B)** Horizontal displacements using stable surface LiDAR points. Each black arrow represents the average displacement of an area of 2.25 km^2. Arrow directions represent the mean displacement direction, and the length of the arrow represents the mean displacement magnitude. Ellipses show the error multiplied by 30 for visualization, where East error represents the error in the east component and North error represents the error in the north component. Red arrows are horizontal displacements using the rates from the GNSS stations for 19 years. Base map imagery from QuickMapServices - QGIS (Map data ©2015 Google)

4.3 Vertical displacement from LiDAR

In this section, we show the results for vertical displacement using ICP and Vertical DEM differencing. These two methodologies give us similar results: there is subsidence across the complete region and subsidence is larger in the northern block than in the southern block. Some regions show uplift mostly in the southern block and it is localized in areas where InSAR time series have smaller rates (Figs. 4, 5, 7, 8). Results from ICP (Fig. 7A, 7B) show the estimated vertical motion for an area of 2.25 km^2. In this case, subsidence increases from southwest to northeast. ICP using LiDAR ground points (Fig. 7A) indicates that the uplift region on the southern block is small while the northern block experienced greater subsidence.

With ICP with LiDAR points on stable surfaces, we detected that the uplift area is larger: mostly across the southern block. Again, we estimate more subsidence in the northern block than in the southern block (Fig. 7B). The errors for this experiment are larger compared to the ones found using LiDAR ground points, although this was expected due to the lack of stable surfaces in 1999 in comparison to the ones found in 2018.

In comparison to the SJB1 GNSS station, which shows a vertical motion between 1999-2018 of -25.65 mm, the results using LiDAR ground points are almost four times larger than the

estimates from the station, and the results from the points of the stable surface are almost two times larger. It is worth to remember that since the GNSS station is anchored at some unknown depth, each tool may be measuring different processes.

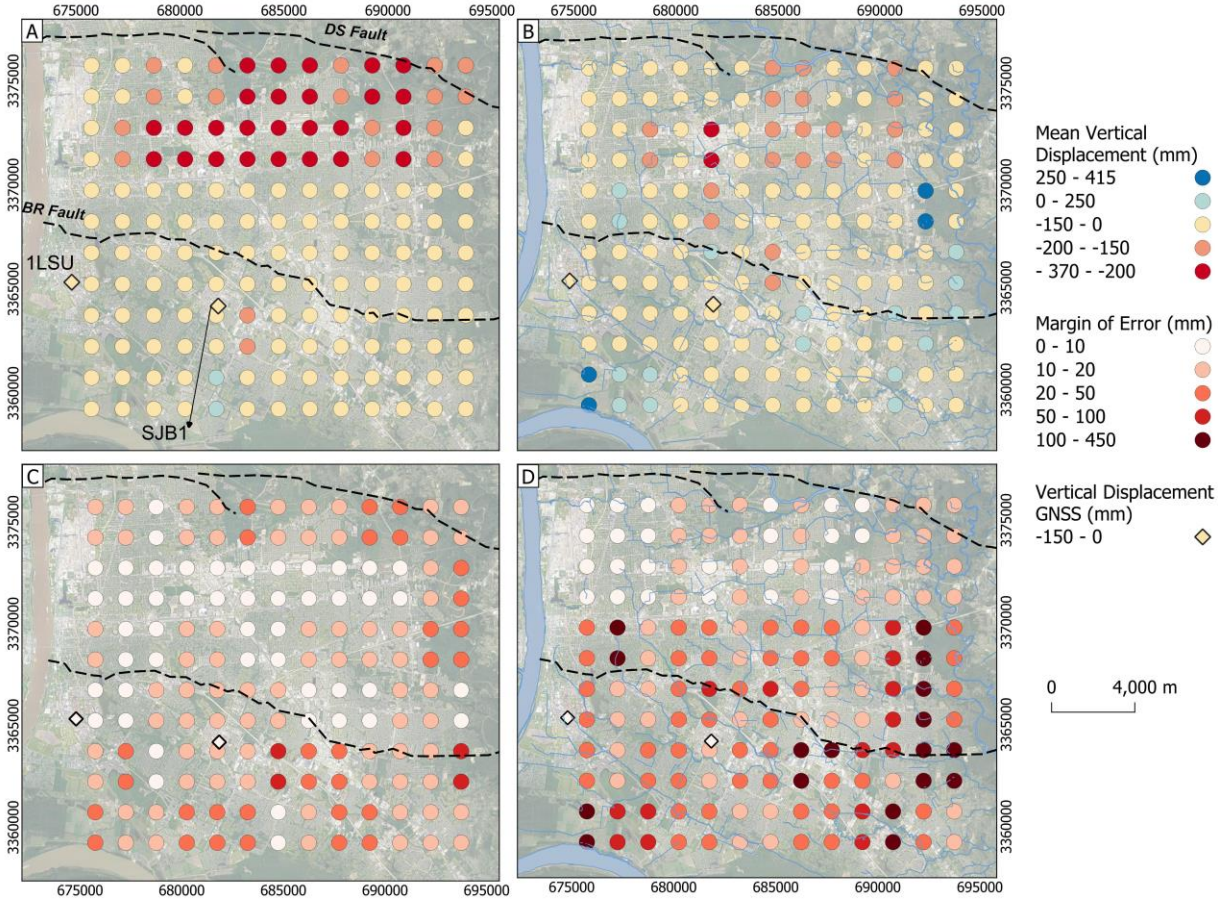

Figure 7: Vertical displacement calculated from ICP algorithm. **(A)** Mean displacement using LiDAR ground points. **(B)** Mean displacement using stable surfaces LiDAR points. **(C)** Margin of error of the results for (A). **(D)** Margin of error of the results for (B). Each circle in A and B represents the mean displacement of an area of 2.25 km^2. Errors in C and D are calculated as the margin of error with respect to the mean. Rhombus are the vertical displacement calculated using rate from the GNSS CORS stations for 19 years. Base map imagery from QuickMapServices - QGIS (Map data ©2015 Google). Systematic errors are calculated as the average difference between the fourth row from north to south of (A) and (B).

We calculated Vertical DEM differencing 1) without co-registration; 2) with co-registration using ground points; and 3) with co-registration using points on stable surfaces. Results without co-registration show mean displacements per block larger than 300 mm in the 19 years of analysis and more extreme values at individual locations; these values are not coherent with other estimates nor the features in the area. We, therefore, only keep the results from co-registered DEMs. We are just presenting the results for co-registration with ground points (Fig. 8) because these results and the ones co-registered with stable surface points present similar

patterns, but the sample of points here is larger for co-registration. The mean vertical displacement for the northern block is -211.86 mm and for the southern block it is -133.09 mm. Errors are found in Table 2. For this analysis the errors (MOE) are small due to the large number of pixels on each block. These results show again more subsidence in the northern block than in the southern block. Empty pixels in Figure 8 do not have results because there are water bodies, high vegetation density, or the values were below the propagated error for each subarea of 2.25 km^2. Insets show areas of interest for the discussion section.

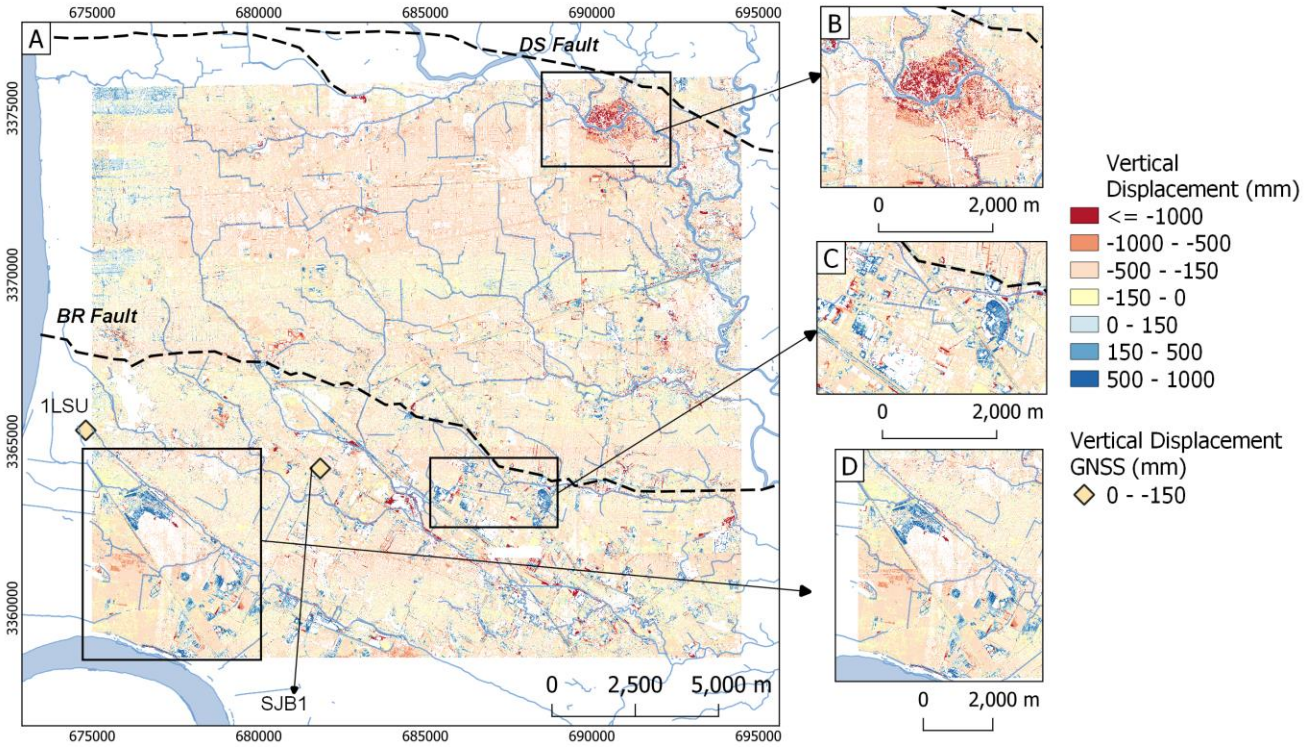

Figure 8: Vertical displacements calculated from Vertical DEM differencing. **(A)** Vertical displacements calculated the co-registered DEM using results from ground points. **(B, C, D)** Some areas of interest discussed in the text.

All our estimates and main statistics are summarized in Table 2. These values are averaged estimates for the whole block calculated using the results in that area, rather than individual locations. This table does not include the residual systematic errors that may affect the data for InSAR and LiDAR (Section 3.5). The former errors may be considered when looking at individual locations.

Table 2: Main statistics per block for each tool. MOE stands for Margin of Error. Numbers marked with a * refer to values derived from the estimates. These numbers do not have an estimated error and are for comparison purposes. All the values are in NAD83. The InSAR displacements correspond just to the period indicated in the column Time Span. The LOS rates for the GNSS stations are the projections of the rates using the parameters for each satellite.

PSI (LOS direction)						
Dataset	**Time Span**	**Block**	**Mean velocity (mm/y)**	**Median velocity (mm/y)**	**MOE of the mean velocity (mm/y)**	**Mean displacement (mm)**
EnviSAT	2004-2010	Northern	-10.869	-11.225	0.0384	-65.214*
		Southern	-8.030	-7.839	0.0614	-48.181*
Sentinel-1	2017-2020	Northern	-13.65	-13.645	0.00471	-40.96*
		Southern	-10.559	-10.82	0.00895	-31.68*
ICP						
Dataset	**Direction**	**Block**	**Mean velocity (mm/y)**	**Mean displacement (mm)**	**Median displacement (mm)**	**MOE of the mean displacement (mm)**
Ground point cloud	Up	Northern	-8.385*	-159.313	-140.9	13.8
	North		2.51*	47.66	49.54	9.26
	East		13.964*	265.31	269.41	10.32
	Up	Southern	-5.124*	-97.352	-101.4	8.03
	North		1.162*	22.072	27.04	8.45
	East		13.845*	263.05	259.41	10.72
Stable point cloud	Up	Northern	-5.023*	-95.433	-117.89	19.671
	North		2.52*	47.866	25.04	13.155
	East		14.44*	274.389	295.9	15.638
	Up	Southern	-2.391*	-45.422	-82.89	28.75
	North		2.845*	54.056	56.04	12.192
	East		11.89*	225.9	225.9	19.595
DEM differencing						
Dataset	**Direction**	**Block**	**Mean velocity (mm/y)**	**Mean displacement (mm)**	**Median displacement (mm/y)**	**MOE of the mean displacement (mm/y)**
DEM's from Ground point clouds	Up	Northern	-11.15*	-211.859	-207.565	0.00014
	Up	Southern	-7.005*	-133.09	-167.9	0.00025
GNSS						
Station	**Direction**	**Block**	**Mean velocity (mm/y)**		**Mean displacement (mm)**	
1LSU	Up	Southern	-4.31		-81.89* (1999-2018)	
	North		2.66		50.54* (1999-2018)	
	East		13.39		254.41* (1999-2018)	

	LOS EnviSAT		-9.81	-58.86* (2004-2010)
	LOS Sentinel		-10.89	-32.6* (2017-2020)
SJB1	Up	Southern	-1.35	-25.65* (1999-2018)
	North		2.22	42.18* (1999-2018)
	East		13.69	260.11* (1999-2018)
	LOS EnviSAT		-7.23	-43.38* (2004-2010)
	LOS Sentinel		-8.4	-25.2* (2017-2020)

583

584 **5 Discussion**

585 **5.1 InSAR time series and LiDAR differencing measurements**

586 We created time series with the PSI method using EnviSAT data between 2004 and 2010 and
587 Sentinel-1 data acquired between 2017 and 2020. The rates and displacements calculated with
588 this method are presented in the LOS direction. We are aware that there are significant horizontal
589 displacements in the study area because the two GNSS stations and LiDAR-ICP results show
590 displacements towards the north and east directions (Fig. 6). Owing to the horizontal
591 displacements, we cannot isolate vertical displacements from InSAR because we only have one
592 geometry for the SAR acquisitions, but we can compare the observations in the LOS direction to
593 the vertical results from LiDAR (Zhong et al., 2022). PSI uses persistent scatterers on the surface
594 to estimate their deformation, making this methodology appropriate for urban areas such as
595 Baton Rouge (e.g., Ferretti et al., 2004). One must be cautious, however, with the interpretation
596 of these results because they incorporate the signal of all the processes affecting the base of the
597 persistent scatterer (e.g., Crosetto et al., 2016). One of the processes that may shape the results
598 from the InSAR time series is the seasonal variations from the hydrological cycle (Li et al.,
599 2020); for both datasets, most of the images were acquired during dry periods between October
600 to April (Table S1). Then, if there is any elastic deformation caused by seasonal changes in water
601 mass, it would appear more positive than negative due to the acquire dates of our images.
602 Seasonal loading may increase the rates (Figs. 4, 5). If the rates are influenced by seasonal
603 rebound, then subsidence may be larger than the rates reported with InSAR time series, based on
604 comparison to hydrological models (e.g., Puskas et al., 2017; Chen et al., 2023).

The two LiDAR surveys used here were acquired over similar seasonal conditions. Then, ICP and LiDAR differencing probably are measuring net changes between the surveys with little impact of the seasonal cycles, although uncertainties must be considered for individual locations. The results are more affected by the LiDAR point cloud with the worst resolution: the 1999 survey.

One of the advantages of using LiDAR data is that it allows one to separate the information into surfaces of interest such as ground points and stable surfaces. We used this approach (Fig. 6 and 7) to estimate the displacement in the three components of surfaces that are at different elevations or anchored in the subsurface. Just as InSAR, these methods measure signals of all the processes that affect the base of the point. Here we take advantage of the spatial resolution of LiDAR and averaged pixels to improve the results that can be affected by the low vertical accuracy of the 1999 survey. With LiDAR we estimate the vertical and horizontal components of displacement between the two surveys using ICP, which goes a step further than just the estimates of vertical motion taken by Zhong et al. (2022). ICP estimates indicate that most of the horizontal motion is towards the east in both blocks (Fig. 6), agreeing with the GNSS stations in the area. Nevertheless, the horizontal displacements estimated with stable ground points (Fig. 6B) have more variations and seem to indicate more motion towards the north in comparison to the ones estimated with ground LiDAR points, particularly near the eastern segment of the BRF (Fig. 6). It is worth noting that the difference between the results from ground and stable LiDAR points may indicate anomalies near the fault segment at different depths, but also may be caused by the lack of stable surfaces in some areas in 1999 before rapid urban growth between 2005-2010 (Supplemental Material – gif 1). The sharp change between the results using LiDAR ground and stable points in the northern block (Fig. 7) may be caused by residual systematic errors left after co-registration of the surveys (Section 3.6). This area marks the edge between files from the 2018 point cloud. Systematic errors similar to the ones observed here have been reported in previous research with topographic LiDAR data (e.g., Anderson, 2019).

5.2 Comparison of LiDAR differencing, InSAR time series and GNSS records

LiDAR results, ICP and differencing all indicate that the northern block is subsiding faster than the southern block with respect to the 1LSU GNSS station. The InSAR time series also indicates that the northern block is moving away from the satellite faster than the southern block. It is, therefore, reasonable to assume that the vertical motion is dominating the

measurements, and it is very likely that the north component is negligible (e.g., Samieie-Esfahany et al., 2010). From InSAR measurements, it is possible to see that the BRF serves as a boundary between the areas of rapid and slow subsidence (Fig. 4 and 5). This behavior, however, contradicts the long-term displacement of the down-to-south normal fault from seismic imaging (e.g., Fig. 1).

The mean vertical rates from ICP vary between -8.4 to -5 mm/y in the northern block and -5.1 to -2.4 mm/y in the southern block. Sentinel-1 rates in the LOS direction are larger than the ICP vertical rates by ~5 mm/y in both blocks. We can, therefore, infer that the results are not just comparable in magnitude but consistent, and that the northern block is subsiding faster than the southern block.

In the southern block, there are two GNSS stations. We used the 1LSU station to tie the results and SJB1 for comparison. These stations show that the southern block is subsiding and moving horizontally E-NE in the NAD83 reference frame. This motion agrees with the direction of the ICP results. The E-NE horizontal motion from the GNSS stations and ICP is likely due to the definition of the NAD83 reference frame with plate fixed as indicated by horizontal velocity models for North America (e.g., Snay et al., 2013; Robin et al., 2020). These results also suggest shallow vertical slip rather than rotational slip along the BRF.

The velocity from Sentinel-1 InSAR time series on the building hosting SJB1 ranges between -9 to -12 mm/y in the LOS direction, while SJB1 has a velocity of -8.40 mm/y (Fig. 4). This difference can be caused by the length of the time series of each case; SJB1 rate is calculated with data since 2010 while InSAR only covers 2017-2020. Changes in the station may also play a role, but still, there is agreement among all the three tools. The two nearby GNSS stations have different vertical motion rates (Section 2.4, Table 2; Fig. S3). The difference in amplitude may appear as uncertainty in the InSAR data after tying to GNSS, whereas it is most likely a local geological effect caused by the local response to groundwater changes. SJB1's magnitude is better replicated by the results with stable LiDAR points (Fig. 7 and Table 2).

5.3 Relation with anthropogenic activities

Results from LiDAR differencing provide good estimates to detect trends of changes in small areas due to their high spatial resolution. These results show the spatial trends of the complete study area and the changes caused by human construction. For instance, the

construction of the FedEx facility in 2014, the Ochsner Medical Complex in 2017, the Woman's hospital in 2010, and some new home complexes between 2006-2017 are seen in Figures 8C and 8D. Although these changes are visible with LiDAR, we consider that urban growth and new constructions are not the main factors decelerating the rates in the southern block, or accelerating them in the northern block, because urban growth has occurred across Baton Rouge (Supplemental Material – gif, Fig. S6). There are multiple examples of construction with similar characteristics in the northern block that do not affect the general spatial trend of the fault block (Fig. S6). The 2000, 2010, and 2020 censuses indicate that the city's population has increased by almost 10% (~44.000 new habitants) with most of this increase occurring during the first decade and soon after Katrina (U.S. Census Bureau, 2003; 2012; 2021). The areas in the southern block with smaller rates are recorded in LiDAR ICP, vertical DEM differencing, and in both InSAR time series.

During the study period 2034 water wells were active, with 592 of them extracting water for multiple purposes (Fig 9, Table 1). The remaining wells monitored groundwater quality and level mostly near industrial wells, close to areas of injection or oil and extraction, and near the western and middle segments of the BRF. Most of the groundwater in East Baton Rouge is used for industrial and public supply. These uses are recognized to cause most of the decline of the groundwater levels in the region and saline intrusions near the BRF (Tomaszewski et al., 2002; Anderson et al., 2013). Groundwater studies indicate the aquifers in the northern block recharge from infiltration in areas north of the DSF (Tomaszewski et al., 2002; Vahdat-Aboueshagh and Tsai 2021), while the aquifers in the southern block are filled mostly with saline water from the GOM (Fig. 1). It is known that groundwater withdrawal in the Baton Rouge district surpasses recharge, causing the decline in groundwater levels (White, 2017). There are more water wells in the northern block than in the southern block for almost all uses due to the salinity charge (Fig. 9A). Also, most wells are at deeper depths in the northern block (Fig. 9B). The mean depth for industrial and public supply wells is between 400-500 m, probably reaching the deeper sand layers (1500 and 2000-ft sands). These aquifers have been greatly affected by pumping water (Tomaszewski et al., 2002; Nasreen, 2003; Elshall et al., 2013), and have developed cones of depression (Chen et al., 2023). On the other hand, the southern block has fewer water wells extracting water, which is more saline, and are at shallower depths. Our results support the hypothesis that the northern block is part of a regional depression cone caused by water

extraction and observed in previous groundwater models (e.g., Chen et al., 2023). This may explain the general trend of subsidence displacements increasing from south to north with LiDAR and in the LOS direction with InSAR time series.

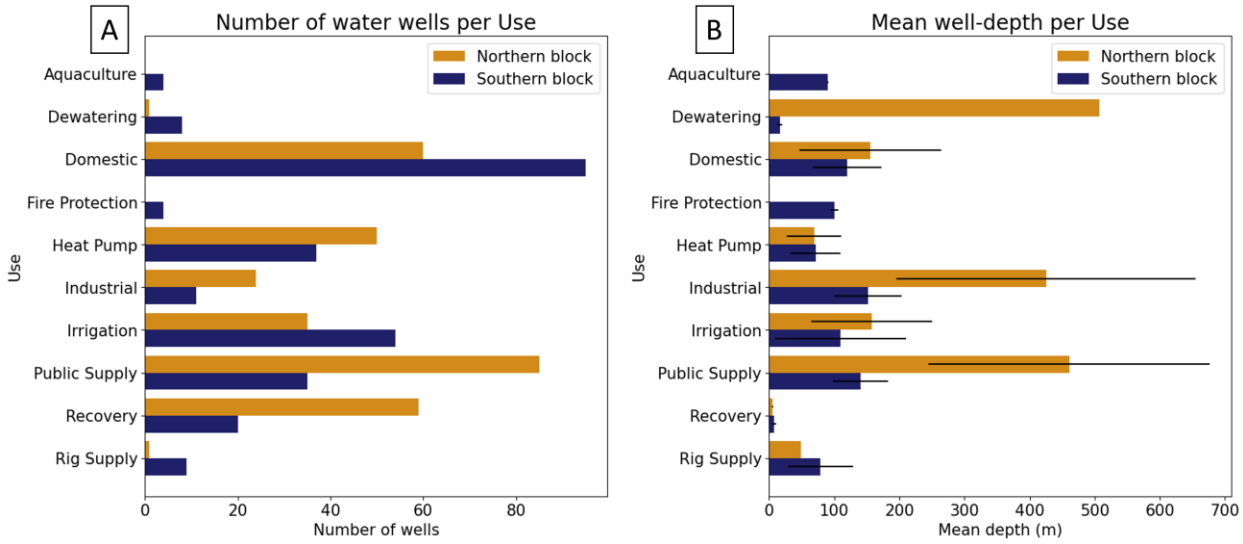

Figure 9: Water well statistics per block in the study area. **(A)** Number of wells per use. **(B)** Mean depth of water wells per use. Lines indicate standard deviation of the well depth values. Well data from the Louisiana Department of Natural Resources (SONRIS), (n.d.).

The relationship between groundwater withdrawal and subsidence is known and supported by several studies globally (e.g., Guzy and Malinowska, 2020; Fiaschi and Wdowinski, 2020). Jones et al., (2016) concluded that groundwater withdrawal caused subsidence in the Michoud area in New Orleans. They found that areas around chemical plants or refinery facilities with water wells have larger subsidence rates than areas without these wells. The area with largest subsidence in our study area was detected with LiDAR methods (Fig. 7 and 8B), while in InSAR time series it is masked by dense vegetation. This region does not have water wells, but there are 15 water wells that were active during the study period within a radius of 2 km, seven of which are of domestic use at the north and east, five for public supply in the west and south, three for irrigation in the west direction (Fig. S7). Another factor that should not be ignored is the proximity to the Comite river at the eastern edge of the study area (Fig. 3) and its interaction with the aquifers in this area. Chen et al. (2023) argue that the Comite river does not have important interactions with the Southern Hills aquifer system, although locally this area remains an open question.

Figures 8C and 8D show the areas with the smallest subsidence displacements in the study area. These areas have most of the injection and oil/gas extraction wells (Fig. 2, S4, Table 1). Ten of these wells injected saline waters at depths between 1445-3155 m. The other injection wells are at ~15 m depth and are not included in these areas. Multiple studies have shown that injection of fluids can increase pore pressure at depth which can diffuse and cause local uplift (e.g., Teatini et al., 2011; Anderson et al., 2013; Shirzaei et al., 2016). Shirzaei et al., (2016) related injection of fluids with large surface displacement and earthquakes in Texas. For their model they calculated a volume change of 700.000 m^3/y which is close to the injection volume of their area. Consequently, an increase in subsurface pressure caused by injection can be an explanation for the slower displacements and rates in the southern block (e.g., Fig, 4C point P6). We compare the depth and injected volume of the injection wells with our results (Fig. 10) to see if there is any evidence of change of the surface that could be related to them. Our study area does not have a total injection above 300,000 m^3/y during the study period (Fig. 10), suggesting that pressures are not yet large enough to induce earthquakes.

One interesting example of the possible signals of injection are the wells identified as 971098 and 188322 (Fig. 10). They are separated by ~ 200 m and both injected a similar volume of saline water. The first one injected water before 2008, while the second experienced fluid injection between 2011 and 2019. Besides the period of injection, these two wells differ in the depth of injection: Well 971098 bottoms at ~1500 m whereas 188322 bottoms at ~3000 m. The two injection depths fill different sand bodies, but the shallower well is expected to contribute more to the observed relative uplift of the southern block; there is not a strong signal from the deeper well in the Sentinel-1 dataset. This was expected due to the disposal depth of the wells. Another example is the four wells in the western part of the study area (Fig. 10). The distance among these is less than 1 km. The depth of these wells varies between ~1500 to ~3000 m. The complete area seems to be moving at slower rates than the northern block, but it is not possible to disentangle the signal caused by each injection well. Our observations indicate that the BRF may be acting as a barrier preventing flow of the injected fluids to the northern block (e.g., Shirzaei et al., 2016).

We perform a similar comparison with the oil and gas wells (Figs. S4, S8). All of these wells have bottom hole depths deeper than 1700 m, and most are near the injection wells which are at shallower depths. It is not possible to say whether these wells are causing any change in our

results, and therefore we cannot conclude that oil and gas extraction during the study period caused any change on the surface.

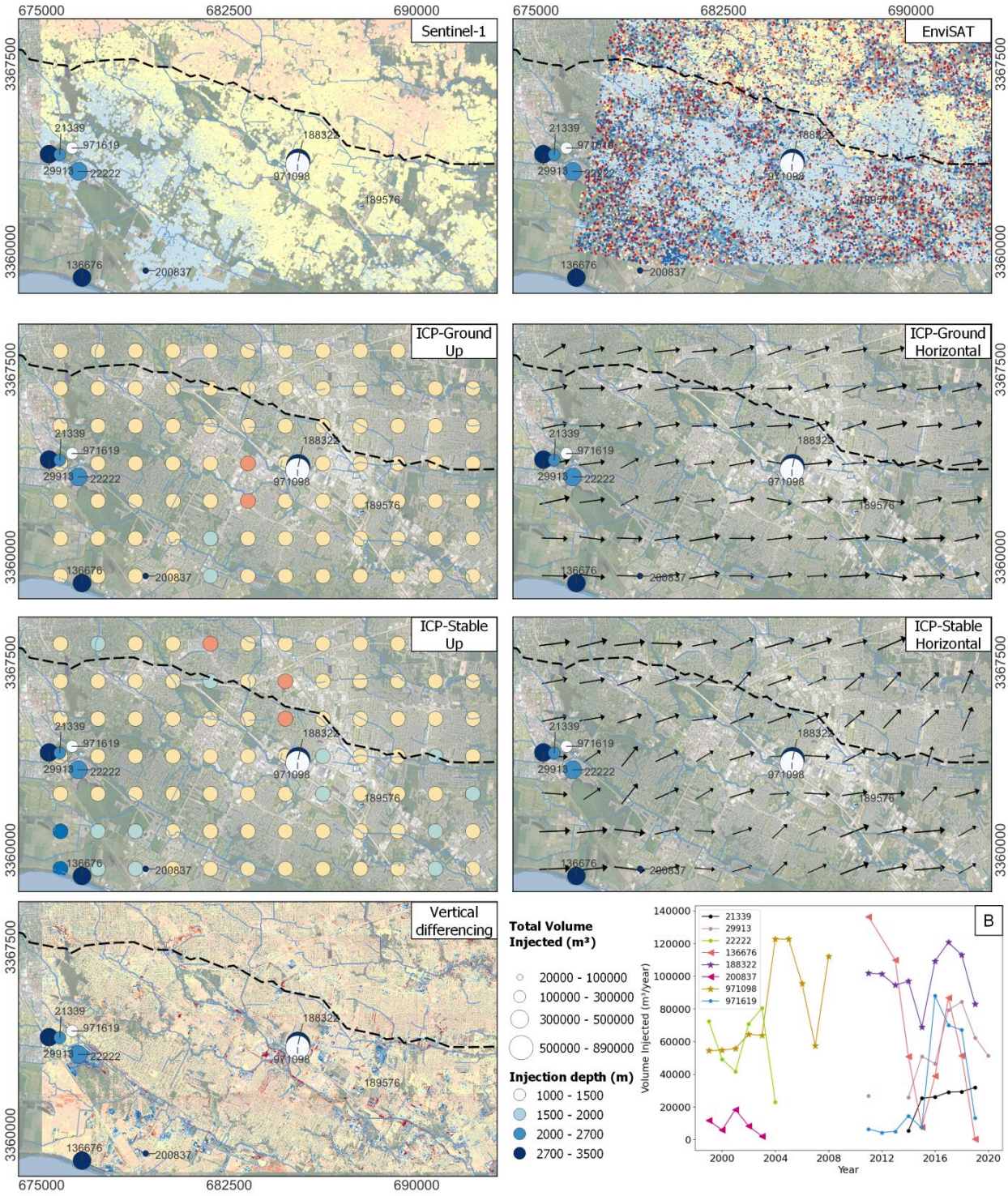

Figure 10: Injection volumes and depth shown in all our results. **B)** Time series of volumes injected by each well in the study area between 1999 and 2020.

5.4 Geological factors

The study area has multiple factors that may contribute to vertical crustal movement that are difficult to deconvolve, but sediment compaction is minimal. Our results from InSAR time series and LiDAR show that the entire area is subsiding, but that the BRF marks the boundary between faster and slower subsiding areas (Figs 4-8). These results agree with groundwater models of the region. The sharp change in vertical crustal movement along some sectors of the BRF suggests that BRF remains a hydrological divide, but we cannot determine whether parts or all the fault slipped episodically or continuously between 1999 and 2020. The rates that we determined (Table 2) are two orders of magnitude larger than the time-averaged fault slip rate from Shen et al. (2017) (~ -0.02 mm/y) and are comparable or larger than the ~3 mm/y from Hopkins et al., (2021) for some segments of BRF. The correlation of changes in vertical crustal motions with injection and water wells indicates that anthropogenic activities have increased BRF slip rates, but we cannot conclude much about the DSF due to the lack of information in the area.

We present four examples of individual structures' motion along the BRF (Fig. S9; Supplemental material - T2). It is important to highlight the examples in the center area of the fault that show more motion than those near the eastern and western limits, although the foundations of examples are unknown and, in some cases, the number of PSIs is very small. We recommend further investigation of individual structures with InSAR time series and/or ground leveling campaigns.

Horizontal displacement from ICP in the eastern portion of the BRF shows an apparent change of direction (Fig 6). Despite the large uncertainties, this can be an area of future research because 1) the Nesser and Siegen oil fields are nearby in the southern block and were exploited during the study period, 2) in August of 2016, the Amite River (Fig. 3) flooded affecting the eastern part of the study area which may influence the time-averaged estimates in the area.

5.5 Future Implications

Vertical crustal motion occurred in the Baton Rouge sector of the GOM passive margin since 1999, as detected here with InSAR and LiDAR methods, and corroborated by sparse GNSS data. These vertical crustal movements may be an indicator of groundwater storage changes and recharge characteristics for the aquifers under the study area. These motions may also indicate how injection at shallow depths is deforming the surface. The BRF zone serves as a boundary

between two differentially subsiding blocks, indicating that it may also separate distinct hydrographic domains, and that it localizes differential motion. Hydrological studies indicate that the aquifers in the northern block are more affected by groundwater withdrawal than those in the south (e.g., Elshall et al., 2013). The subsidence rates in the northern block increase from the BRF towards the DSF, and in the southern block subsidence increases south of the BRF, where saline water infiltrates sand bodies and where saline wastewater is injected (Nasreen, 2003; Elshall et al., 2013; White, 2017). Our results agree with recent groundwater change models of Chen et al. (2023). They show that the average groundwater levels between 2004 and 2020 were low (-10 to -20 m) in Baton Rouge between the BRF and the DSF. This area is part of the local cone of depression caused by the large water extraction of deep aquifers at 400-900 m depth. Our results in the northern block may be the surface expression of the changes in groundwater storage (i.e., the cone of depression) caused by the decline of groundwater levels showed on Chen et al., (2023).

East Baton Rouge is one of the most populated parishes in Louisiana and likely its population will grow as it has done it in the last 20 years (U.S. Census Bureau, 2003; 2012; 2021). Besides, due to climate changes expected for the ongoing century in the GOM (Pendleton et al., 2010; Frederikse et al., 2020; Dangendorf et al., 2023), coastal retreat from regions vulnerable to storm surge and wind damage from hurricanes will continue to drive population growth (e.g., Qiang and Lam, 2016) as has happened before (Sastry, 2009). Simultaneously, as the population grows, water consumption likely will increase. Considering vertical surface changes as a proxy for groundwater level and storage changes, it is important to protect the aquifers underlying the area from saline water intrusions and groundwater level decline. These actions will also protect the surface from non-natural changes.

There are many wells whose purpose is to monitor local groundwater, but just two GNSS stations to study surface elevation changes; they are wholly inadequate to track BRF movement. The localized fault slip along the BRF and differential ground subsidence motivates continuous monitoring at local and regional scales to track surface elevation changes associated with fluid extraction and injection.

6 Conclusions

This study presents a detailed regional panorama of the relationship between injection and extraction of fluids and vertical and horizontal surface displacements. We also show how geodetic methods can be used to estimate vertical and horizontal displacements in areas with slow motions for the first-time using LiDAR data with the ICP algorithm. InSAR time series with PSI is a suitable method for urban areas such as Baton Rouge and shows similar results to LiDAR in the LOS direction after GNSS corrections. We verify our results using ground measurements from permanent GNSS stations. The agreement of the results from the three datasets on the same reference system offers insight into the reliability of LiDAR to estimate vertical and horizontal motion. We reiterate the need for more GNSS stations in the area, particularly in the northern block, to adequately track the motion of the BRF and to better constrain the results from other geodetic methods.

We selected East Baton Rouge as the study area because the deformation signal caused by fault slip and anthropogenic activities should control vertical ground motion. Our results show that the entire area is subsiding, but subsidence reverses the long-term, down-to-the-south displacement. We observe that the BRF divides the study area into two different regions of mostly human-controlled subsidence: 1) Subsidence in the northern block is likely controlled by groundwater level changes caused by pumping and it is sinking faster than the southern block showing a cone of depression. These results are supported by recent groundwater models. 2) Subsidence in the southern block, which is influenced by the injection of fluids at shallow depths that may be causing volumetric expansion and less water pumping. It is important to remember that seasonal contributions can influence the results from InSAR time series, and it is something to consider in future analysis. Horizontal motions estimate from ICP show that the area is moving to the east with a small displacement to the north. This agrees with the estimates from GNSS.

Considering the future climate change scenarios where population displacement and water scarcity are likely, it is important to consider these observations for future city planning to ensure the conservation and protection of the aquifers in the area, and to minimize the effects of saline infiltrations through the BRF.

Acknowledgments

CH and CE were supported by funds from the Marshall-Heape endowment to Tulane University and from training opportunities offered by UNAVCO (Earth Scope). CH and CE grateful acknowledge support from the Marshall-Heape endowment to Tulane University. CH thanks the conversations with JL. Whitten and K. Materna about the development of this work and S. Villamarin about the statistical background. This manuscript benefited from conversations with R. Arrowsmith. Thanks to reviewers Artur Guzy and the other anonymous reviewers for the feedback that helped to improve this research.

Open Research

Data Availability Statement

LiDAR data from 1999 is stored and distributed by the Atlas: The Louisiana Statewide GIS (https://maps.ga.lsu.edu/lidar2000/). LiDAR data from 2018 is stored and distributed by the USGS Server through The National Map Download Manager (https://apps.nationalmap.gov/downloader/).

EnviSAT SAR images were retrieved from the Earth Observation Catalogue (https://eocat.esa.int/sec/#data-services-area). Sentinel-1 SAR images from the Copernicus Open Access Hub (https://scihub.copernicus.eu/dhus/#/home). Both property of the European Space Agency.

GNSS information was processed by the Nevada Geodetic Laboratory (Blewitt et al., 2018; http://geodesy.unr.edu/NGLStationPages/gpsnetmap/GPSNetMap.html).

Data from water, injection, and extraction wells is stored in the Strategic Online Natural Resources Information System property of the Louisiana Department of Natural Resources (http://sonris-www.dnr.state.la.us/gis/agsweb/IE/JSViewer/index.html?TemplateID=181).

LiDAR and InSAR results are available in a data repository (Hurtado-Pulido et al., 2023).

Software Availability Statement

LiDAR data was filtered to create stable surface clouds and DEMs were created using the Point Data Abstraction Library (PDAL, 2018). The ICP algorithm was run using the MATLAB code created by Scott et al. (2020) that uses the LIBICP software (Geiger et al, 2012). The Geomorphic Change Detection software (GCD) was used to create the DEMs of Differences (Wheaton et al., 2010). InSAR time series were processed using SARscape (2021) software.

875 Spatial analysis and maps were done with QGIS v. 3.18 (2018). Figures were done using
876 Matplotlib on Python (Hunter, 2007).

877 **References**

878 Andersons, S., (2019). Uncertainty in quantitative analyses of topographic change: error
879 propagation and the role of thresholding. Earth surface processes and landforms. 44 (5),
880 1015-1033. doi: 10.1002/esp.4551
881 Anderson, C., Hanor, J., Tsai, F., (2013). Sources of salinization of the Baton Rouge aquifer
882 system, Southeastern Louisiana. *Gulf Coast Association of Geological Societies*
883 *Transactions*. 63, 3-12.
884 Blewitt, G., Hammond, W., Kreemer, C., (2018), Harnessing the GPS data explosion for
885 interdisciplinary science. *Eos*, 99, https://doi.org/10.1029/2018EO104623
886 Blum, M., & Roberts, H. (2012). The Mississippi delta region: Past, present, and future. *Annual*
887 *Review of Earth and Planetary Sciences*, 40, 655-683. doi:10.1146/annurev-earth-042711-
888 105248
889 Brook, A., and Ben-Dor, E., (2011). Automatic registration of airborne and spaceborne images
890 by topology map matching with SURF processor algorithm. *Remote Sensing*, 3 (1), 65-82.
891 doi:10.3390/rs3010065
892 Chan, Y., Koo, V., (2008). An introduction to Synthetic Aperture Radar (SAR). *Progress in*
893 *Electromagnetics Research*, 2, 27-60. doi:10.2528/PIERB07110101
894 Chan, A., and Zoback, A., (2007). The role of hydrocarbon production on land subsidence and
895 fault reactivation in the Louisiana Coastal Zone. *Journal of Coastal Research*, 23 (3), 771-
896 786. doi: 10.2112/05-0553
897 Chen, Y., Vahdat-Aboueshagh, H., Tsai, F., Dausman, A., Runge, M., (2023). Unstructured-grid
898 approach to develop high-fidelity groundwater model to understand groundwater flow and
899 storage responses to excessive groundwater withdrawals in the Southern Hills aquifer
900 system in southeastern Louisiana (USA). *Journal of Hydrology: Regional Studies.* 46. doi:
901 10.1016/j.ejrh.2023.101342
902 Church, J., Clark, P., Cazenave, A., Gregory, J., Jevrejeva, S., Levermann, A., Merrifield, M.,
903 Milne, G., Nerem, R., Nunn, P., Payne, A., Pfeffer, W., Stammer D., and Unnikrishnan, A.,
904 (2013). Sea Level Change. In: Climate Change 2013: The Physical Science Basis.
905 Contribution of Working Group I to the Fifth Assessment Report of the Intergovernmental
906 Panel on Climate Change [Stocker, T., Qin, D., Plattner, G., Tignor, M., Allen, S.,
907 Boschung, J., Nauels, A., Xia,Y., Bex V., Midgley, P., (eds.)]. Cambridge University Press,
908 Cambridge, United Kingdom and New York, NY, USA.
909 Crosetto, M., Moserrat, O., Cuevas-Gonzalez, M., Devanthery, N., Crippa, B., (2016). Persistent
910 Scatterer Interferometry: A review. *ISPRS Journal of Photogrammetry and Remote Sensing*.
911 115, 78-89. doi:10.1016/j.isprsjprs.2015.10.011
912 Culpepper, D., McDade, E., Dawers, N., Kulp, M., and Zhang, R., (2019a). Synthesis of fault
913 traces in SE Louisiana relative to infrastructure (Project No. 17GTLSU12). *Transportation*
914 *Consortium of South-Central States*. https://digitalcommons.lsu.edu/transet_pubs/30/

915 Culpepper, D., McDade, E., Dawers, N., Kulp, M., and Zhang, R. (2019b). Data from: synthesis
916 of fault traces in SE Louisiana relative to infrastructure. Retrieved from
917 https://digitalcommons.lsu.edu/transet_data/30
918 Dangendorf, S., Hendricks, N., Sun, Q., Klinck, J., Ezer, T., Frederikse, T., Calafat, F., Wahl, T.,
919 Tornqvist, T., (2023). Acceleration of U.S. Southeast and Gulf coast sea-level amplified by
920 internal climate variability. *Nature Communications.* 14 (1), 1-11. doi: 10.1038/s41467-023-
921 37649-9
922 Dokka, R., (2006). Modern-day tectonic subsidence in Coastal Louisiana. Geology. 34 (4), 225-
923 228. doi: 10.1130/G22264.1
924 Dokka, R. Sella, G., and Dixon, T. (2006). Tectonic control of subsidence and southward
925 displacement of southeast Louisiana with respect to stable North America: *Geophysical*
926 *Research Letters*, 33 (L23308). doi:10.1029/2006GL027250
927 Dokka, R. (2011). The role of deep processes in late 20th century subsidence of New Orleans
928 and coastal areas of southern Louisiana and Mississippi. *Journal of Geophysical Research*.
929 116 (B06403). doi:10.1029/2010JB008008.
930 Durham, C., and Peeples E., (1956). Pleistocene fault zone in southeastern Louisiana. *Gulf Coast*
931 *Association of Geological Societies Transactions*. 6, 65-66.
932 Eddy, D., Van Avendonk, H., Christeson, G., Norton, I., Karner, G., Johnson, C., Snedden, J.,
933 (2014). Deep crustal structure of the northeastern Gulf of Mexico: Implications for rift
934 evolution and seafloor spreading. *Journal of Geophysical Research: Solid Earth*. 119 (9),
935 6802-6822. doi: 10.1002/2014JB011311
936 Elshall, A., Tsai, F., Hanor, J., (2013). Indicator geostatistics for reconstructing Baton Rouge
937 aquifer-fault hydrostratigraphy, Louisiana, USA. *Hydrogeological Journal*. 21 (8), p. 1731-
938 1747. doi: 10.1007/s10040-013-1037-5
939 European Space Agency, (ESA) (2021a). Earth Observation Catalogue – EO CAT. EnviSAT
940 images. Last visited July/2022. Retrieved from https://eocat.esa.int/sec/#data-services-area
941 European Space Agency, (ESA) (2021b). Copernicus Open Access Hub. Sentinel-1 images. Last
942 visited July/2022. Retrieved from https://scihub.copernicus.eu/dhus/#/home
943 Fattahi, H., Amelung, F., (2014). InSAR uncertainty due to orbital errors. Geophysical Journal
944 International. 199 (1). 549-560. doi: 10.1093/gji/ggu276
945 Ferretti, A., Prati, C., Rocca, F., (2001) Permanent scatterers in SAR interferometry. *IEEE*
946 *Transactions on Geoscience and Remote Sensing*. 39 (1), 8–20. doi:10.1109/36.898661
947 Ferretti, A., Novali, F., Burgmann, G., Hilley, G., Prati, C., (2004). InSAR permanent scatterer
948 analysis reveals ups and downs in San Francisco Bay area. *Journal of Geophysical*
949 *Research: Solid Earth.* 85, 317-324. doi: 10.1029/2002jb002267
950 Ferretti, A., Savio, G., Barzaghi, R., Borghi, A., Musazzi, S., Novali, F., Prati, C., Rocca, F.,
951 (2007). Submillimeter accuracy of InSAR time series: Experimental validation. *IEEE*
952 *Transactions on Geoscience and Remote Sensing.* 45(5), 1142-1153. doi:
953 10.1109/TGRS.2007.894440
954 Fiaschi, S., and Wdowinski, S., (2020). Local land subsidence in Miami Beach (FL) and Norfolk
955 (VA) and its contribution to flooding hazard in coastal communities along the U.S. Atlantic
956 coast. *Ocean and Coastal Management*. 187. doi:10.1016/j.ocecoaman.2019.105078

957 Frederikse, T., Landerer, F., Caron, L. Adhikari, S., Parkes, D., Humphrey, V., Dangendorf, S.,
958 Hogarth, P., Zanna, L., Cheng, L., and Wu, Y., (2020). The causes of sea-level rise since
959 1900. *Nature*. 584 (7821), 393–397. doi:10.1038/s41586-020-2591-3
960 Gagliano, S., Meyer-Arendt, K., Wicker, K., (1981). Land loss in the Mississippi River deltaic
961 plain. *Gulf Coast Association of Geological Societies Transactions*. 31, 295-300
962 Gagliano, S., Burton Kemp III, E., Wicker, K., and Wiltenmuth, K., (2003a). Active geological
963 faults and land change in southeastern Louisiana (Contract No. DACW 29-00-C-0034). *U. S.*
964 *Army Corps of Engineers*. https://biotech.law.lsu.edu/katrina/govdocs/faults.pdf
965 Gagliano, S., Burton Kemp III, E., Wicker, K., Wiltenmuth, K., and Sabate, R., (2003b). Neo-
966 tectonic framework of southeast Louisiana and applications for coastal restoration.
967 Transactions of the 53rd *The Gulf Coast Association of Geological Societies and the Gulf*
968 *Coast Section SEMP*. 262-272
969 Gasparini, N, Fischer, G, Adams, J, Dawers, N., Janoff, A., (2015) Morphological signatures of
970 normal faulting in low-gradient alluvial rivers in South-eastern Louisiana, USA. *Earth*
971 *Surface Processes and Landforms*. 41, 642-657. doi: 10.1002/esp.3852
972 Geiger, A., Lenz, P., and Urtasun, R., (2012). Are we ready for autonomous driving the KITTI
973 vision benchmark suite. 2012 IEEE Conference on Computer Vision and Pattern
974 Recognition. 3354-3361. doi: 10.1109/CVPR.2012.6248074. [Computer software]
975 http://www.cvlibs.net/software/libicp/
976 Goldstein, R., Zebker, H., Werner, C., (1988). Satellite radar interferometry: Two-dimensional
977 phase unwrapping. *Radio Science*. 23 (4), 713-720. doi:10.1029/RS023i004p00713
978 Guzy, A., Malinowska, A., (2020). State of the art and recent advancements in the modelling of
979 land subsidence induced by groundwater withdrawal. *Water*. 12 (7). doi:10.3390/w12072051
980 Hooper, A., Zebker, H., Segall, P., Kampes, B., (2004). A new method for measuring deformation
981 on volcanoes and other natural terrains using InSAR persistent scatterers. *Geophysical*
982 *Research Letters*. 31 (23), L23611. doi:10.1029/2004GL021737.
983 Hopkins, M., Lopez, J., Songy, A., (2021). Coastal Subsidence Due to Faults: Insights from
984 Elevation Profiles of Vehicular Bridges, Southeastern Louisiana, U.S.A. *Journal of Coastal*
985 *Research*. 38(1), 52-65. doi:10.2112/JCOASTRES-D-21-00015.1
986 Hunter, J., (2007). Matplotlib: A 2D Graphics Environment. Computing in Science &
987 Engineering. 9 (3), 90-95. doi:10.5281/zenodo.592536
988 Hurtado-Pulido, C., Amer, R., Ebinger, C., Holcomb, H., (2023). Geodetic displacement data
989 from Airborne-LiDAR data and Time Series InSAR: Baton Rouge Case Study [dataset]. doi:
990 10.5281/zenodo.8187870
991 Jankowski, K., Törnqvist, T., Fernandes, A., (2017) Vulnerability of Louisiana's coastal wetlands
992 to present-day rates of relative sea-level rise. *Nature Communication*. 8 (14792).
993 doi:10.1038/ncomms14792
994 Jones, C., An, K., Blom, R., Kent, J., Ivins, E., and Bekaert, D. (2016). Anthropogenic and
995 geologic influences on subsidence in the vicinity of New Orleans, Louisiana. *Journal of*
996 *Geophysical Research: Solid Earth*. 121 (5), 3867– 3887. doi:10.1002/2015JB012636
997 Karegar, M., Dixon, T., Malservisi, R., (2015). A three-dimensional surface velocity field for the
998 Mississippi Delta: Implications for coastal restoration and flood potential. *Geology*. 43 (6),
999 519-522. doi:10.1130/G36598.1

1000 Karegar, M., Dixon, T., Malservisi, R., Kushe, J., and Engelhart, S., (2017) Nuisance flooding
1001 and relative Sea-Level Rise: the importance of present-day land motion. *Science Reports*. 7
1002 (111997). doi:10.1038/s41598-017-11544-y
1003 Karegar, M., Larson, K., Kushe, J., and Dixon, T., (2020) Novel quantifications of shallow
1004 sediment compaction by GPS Interferometric Reflectometry and implications for flood
1005 susceptibility. *Geophysical Research Letters*. 47 (14). doi:10.1029/2020GL087807
1006 Keogh, M., and Törnqvist, T., (2019). Measuring rates of present-day relative sea-level rise in low
1007 elevation coastal zones. *Ocean Science*, 15 (1), 61-73. doi:10.5194/os-15-61-2019
1008 Kuchar, J., Milne, G., Wolstencroft, M., Love, R., Taarasov, L., and Hijma, M., (2018). The
1009 influence of sediment isostatic adjustment on sea level change and land motion along the
1010 U.S. Gulf Coast: *Journal of Geophysical Research*, 123 (1), 780-796.
1011 doi:10.1002/2017JB014695
1012 Kuecher, G., Roberts, H., and Thompson, M., (2001). Evidence for active growth faulting in the
1013 Terrebone delta plain, South Louisiana: Implications for wetland loss and the vertical
1014 migration of Petroleum. *Environmental Geosciences*, 8 (2), 77-94. doi:10.1046/j.1526-
1015 0984.2001.82001.x
1016 Kulp, S., and Strauss, B., (2019). New elevation data triple estimates of global vulnerability to
1017 sea-level rise and coastal flooding. *Nature Communications*. 10 (4844). doi:10.1038/s41467-
1018 019-12808-z
1019 L3Harris. (2014, November). PS Tutorial – version 0.9. Retrieved April 17, 2022, from
1020 https://www.sarmap.ch/tutorials/PS_Tutorial_V_0_9.pdf
1021 L3Harris. (2021, August). PS Tutorial – version 5.6. Retrieved April 17, 2022, from
1022 https://www.sarmap.ch/tutorials/PS_v562.pdf
1023 Li, J., Wang, S., Miche, C., Russell, H., (2020). Surface deformation observed by InSAR shows
1024 connections with water storage change in Southern Ontario. *Journal of Hydrology: Regional*
1025 *Studies*. 27, 100661- 100672. doi:10.1016/j.ejrh.2019.100661
1026 Liang, C., Agram, P., Simons, M., Fielding, E., (2019). Ionospheric Correction of InSAR Time
1027 Series Analysis of C-Band Seintinel-1 TOPS Data. IEEE Transactions on Geoscience and
1028 Remote Sensing. 57 (9), 6755-6773. doi: 10.1109/TGRS.2019.2908494
1029 Love, R., Milne, G., Tarasov, L., Engelhart, S., Hijma, M., Latychev, K., Horton, B., and
1030 Törnqvist, T., (2016). The contribution of glacial isostatic adjustment to projections of sea-
1031 level change along the Atlantic and Gulf coast of North America. *Earth's Future*. 4 (10), 440-
1032 464. doi:10.1002/2016EF000363
1033 Louisiana Department of Natural Resources – Strategic Online Natural Resources Information
1034 System (SONRIS), (n.d.). Data of: Oil/Gas wells, Injection wells, and Water wells
1035 registration [shp format], last visited June/2020. Retrieved from: http://sonris-
1036 www.dnr.state.la.us/gis/agsweb/IE/JSViewer/index.html?TemplateID=181
1037 Louisiana State University - Department of Geography and Anthropology (LSU), (n.d.). LiDAR
1038 data distribution by “Atlas: The Louisiana Statewide GIS.” [LAS format], Baton Rouge, LA.
1039 Last visited: June/2020. Retrieved from: https://maps.ga.lsu.edu/lidar2000/
1040 Mahapatra, P., der Marel, H., van Leijen, F., Samiei-Esfahany, S., Klees, R., Hanssen, R., (2018).
1041 InSAR datum connection using GNSS-augmented radar transporders. *Journal of Geodesy*. 92
1042 (1), 21-32. doi:10.1007/s00190-017-1041-y

McCulloh, R., (2001) Active Faults in East Baton Rouge Parish; Louisiana. *Louisiana Geological Survey*. Public information series n. 8. Available at https://www.lsu.edu/lgs/publications/products/public-information-series.php (Accessed: January 2020).

McCulloh, R., Heinrich, P., (2013). Surface faults of the south Louisiana growth-fault province. *The Geological Society of America*, Special Paper. 493, 37-49. doi: 10.1130/2012.2493(03).

Milliman J., Haq B., (1996). "Sea-Level Rise and Coastal Subsidence: Towards Meaningful Strategies" In: Milliman, J.D., Haq, B.U. (eds) Sea-Level Rise and Coastal Subsidence. Coastal Systems and Continental Margins, vol 2. Springer, Dordrecht. 1-9. doi:10.1007/978-94-015-8719-8_1

Morton, R., Busteri, N., Dennis K. (2002). Subsidence rates and associated wetland loss in south-central Louisiana. *Transactions of the Gulf Coast Association of Geological Societies*. 52, 767-778.

Nasreen, M. (2003) The effect of faults upon ground water flow in the BRF System. [master´s thesis]. [New Orleans (LA)] University of New Orleans. Available at https://scholarworks.uno.edu/td/54 (Accessed: 1 June 2022)

National Academies of Sciences, Engineering, and Medicine (NASEM), (2018). Understanding the Long-Term Evolution of the Coupled Natural-Human Coastal System: The Future of the U.S. Gulf Coast. Washington, DC: The National Academies Press. doi:10.17226/25108

National Geodetic Survey (n.d.). Data from: Finding Survey Marks and Datasheets - LA[shp format], last visited January/2020. Retrieved from https://geodesy.noaa.gov/pub/DS_ARCHIVE/BETA_PRODUCTS/

Nerem, R., Beckley, B., Fasullo, J., Hamlington, B., Masters, D., Mitchum, G., (2018). Climate-change–driven accelerated sea-level rise detected in the altimeter era. *Proceedings of the National Academy of Sciences*. 115 (9), 2022-2025. doi:10.1073/pnas.1717312115

Nienhuis, J., Törnqvist, T, Jankowski1, K., Fernandes, A, Keogh, M., (2017). A new subsidence map for coastal Louisiana. *GSA Today*. 27 (9), 58-59. doi:10.1130/GSATG337GW.1

Nissen, E., Krishnan, A., Arrowsmith, R., Saripalli, S., (2012). Three-dimensional surface displacements and rotations from differencing pre-and post-earthquake LiDAR point clouds. *Geophysical Research Letters*, 39 (16). doi:10.1029/2012GL052460

PDAL Contributors, (2018). PDAL Point Data Abstraction Library. doi:10.5281/zenodo.2556738

Pearson, C., Snay, R., (2013). Introducing HTDP 3.1 to transform coordinates across time and spatial reference frames. *GPS Solutions*. 17 (1), 1-15. doi: 10.1007/s10291-012-0255-y

Pendleton, E., Barras, J., Williams, S., Twichell, D., (2010). Coastal vulnerability assessment of the Northern Gulf of Mexico to sea-level rise and coastal change. *U.S. Geological Survey*. Open-File Report. doi:10.3133/ofr20101146

Penland, S. and Ramsey, K., (1990). Relative Sea Level Rise in Louisiana and the Gulf of Mexico: 1908-1988. *Journal of Coastal Research*. 6 (2), 323-342. Available at https://www.jstor.org/stable/4297682 (Accessed: 20 Marzo 2021)

Penland, S., Beall, A., and Waters, J., (2001) Environmental atlas of the Lake Pontchartrain Basin. *U.S. Geological Survey.* Open-File Report 02-206. Retrieve from https://pubs.usgs.gov/of/2002/of02-206/intro/toc.html

1085 Pindell, J. Kennan, L., (2009), Tectonic evolution of the Gulf of Mexico, Caribbean and northern
1086 South America in the mantle reference frame: An update. In The Origin and Evolution of the
1087 Caribbean Plate, *Geological Society, Special Publication*., edited by Lorente, J., Pindell, J.
1088 328, 1–55. doi:10.1144/SP328.1.
1089 Puskas, C., Meertens, C., & Phillips, D. (2017). Hydrologic loading model displacements from
1090 the National and Global Data Assimilation Systems (NLDAS and GLDAS). *UNAVCO*
1091 *Geodetic Data Service Group*.
1092 Qiang, Y., Lam, N., (2016). The impact of Hurricane Katrina on urban growth in Louisiana: an
1093 analysis using data mining and simulation approaches. *International Journal of*
1094 *Geographical Information Science*. 30 (9), 1832-1852. doi:10.1080/13658816.2016.1144886
1095 QGIS Development Team, 2018. QGIS Geographic Information System. Open-Source Geospatial
1096 Foundation Project. [computer software] http://qgis.osgeo.org
1097 Robin, C., Craymer, M., Ferland, R., James, T., Lapelle, E., Piraszewski, M., Zhao, Y. (2020).
1098 NAD83v70VG: a new national crustal velocity model for Canada. Open File. doi:
1099 10.4095/327592
1100 Samieie-Esfahany, S., Hanssen, R., van Thienen-Visser, K., Muntendam-Bos, A., (2010). On the
1101 effect of Horizontal deformation on InSAR subsidence estimates. In ESA Special
1102 Publication. 677
1103 SARscape [computer software] (2021). Boulder, Colorado
1104 Sastry, N., (2009). Tracing the effects of hurricane Katrina on the population of New Orleans:
1105 The displaced New Orleans residents pilot study. *Sociological Methods and Research*. 38 (1),
1106 171-196. doi:10.1177/0049124109339370
1107 Sawyer, D., Buffler, R., Pilger Jr., R., (1991), "The crust under the Gulf of Mexico basin" In The
1108 Gulf of Mexico Basin, Geological Society of America, ed. by A. Salvador. 53–72.
1109 doi:10.1130/DNAG-GNA-J.53
1110 Scott, C., Arrowsmith, J., Nissen, E., Lajoie, L., Maruyama, T., Chiba, T., (2018). The M7 2016
1111 Kumamoto, Japan, Earthquake: 3-D deformation along the fault and within the damage zone
1112 constrained from Differential Lidar Topography. *Journal of Geophysical Research: Solid*
1113 *Earth*, 123 (7) 6138-6155. doi:10.1029/2018JB015581
1114 Scott, C., Phan, M., Nandigam, V., Crosby, C., & Arrowsmith, R. (2020). On-Demand 3D
1115 topographic differencing implemented in OpenTopography (Version 1.1.0) [Computer
1116 software]. https://github.com/OpenTopography/3D_Differencing
1117 Shen, Z., Dawers, N., Törnqvist, T., Gasparini, N., Hijma, M., and Mauz, B. (2017). Mechanism
1118 of late Quaternary fault throw-rate variability along the north central Gulf of Mexico coast:
1119 implication for coastal subsidence. *Basin Research*. 29 (5), 557-570. doi:10.1111/bre.12184
1120 Shepard, D., (1968). A two-dimensional interpolation function for irregularly spaced data.
1121 Proceedings of the 1968 ACM National Conference. 517 – 524.
1122 https://doi.org/10.1145/800186.810616
1123 Shirzaei, M., Ellsworth, W., Tiampo, K., Gonzalez, P., Manga, M., (2016). Surface uplift and
1124 time-dependent seismic hazard due to fluid injection in eastern Texas. *Science*. 353 (6306),
1125 1416-1419. doi:10.1126/science.aag0262

Shirzaei, M., Freymuller, J., Tornqvist, T., Galloway, D., Dura, T., Minderhoud, P., (2021). Measuring, modeling and projecting coastal land subsidence. *Nature Reviews Earth and Environment*. 2(1), 40-58. doi: 10.1038/s43017-020-00115-x

Snay, R., Freymuller, J., Pearson, C., (2013). Crustal Motion Models Developed for Version 3.2 of the Horizontal Time-Dependent Positioning Utility. Journal of Applied Geodesy. 7 (3), 173-190. doi: 10.1515/jag-2013-0005

Stevenson, D. A., & Agnew, J. D. (1988). Lake Charles, Louisiana, earthquake of 16 October 1983. *Bulletin of the Seismological Society of America*. 78 (4), 1463-1474. doi:10.1785/BSSA0780041463

Teatini, P., Gambolati, G., Ferronato, M., Serrati, A., Walters, D., (2011). Land uplift due to subsurface fluid injection. *Journal of Geodynamics*. 51 (1), 1-16. doi:10.1016/j.jog.2010.06.001

Tomaszewski, D., Lovelace, J., Ensminger, P., (2002). Water withdrawals and trends in groundwater levels and stream discharge in Louisiana. Louisiana *Department of Transportation and Development, and U.S. Geological Survey*, technical report No. 68.

Turner, R., Rabalais, N., (2018). "The Gulf of Mexico." In World Seas: An Environmental Evaluation (Second Edition), Academic Press -Elsevier, edited by Sheppard, C, 445-464. doi:10.1016/B978-0-12-805068-2.09994-0

United States Army Corps of Engineers (USACE) (2001). Data from: Raw LIDAR Elevation Data, UTM 15 NAD83, Louisiana FEMA Project - Phase 1: Amite River Basin. last visited June/2020 Retrieve from: https://maps.ga.lsu.edu/lidar2000/

United States Geological Survey (USGS) (2019), USGS Lidar Point Cloud LA Amite 2018, [LAZ format], last visited July/2022. Retrieve from: https://rockyweb.usgs.gov/vdelivery/Datasets/Staged/Elevation/LPC/Projects/USGS_LPC_LA_Amite_2018_LAS_2019/

U.S. Census Bureau. (2003, October). Louisiana 2000 – Population and Housing units counts (Report No. PHC-3-20). Retrieved from https://www2.census.gov/library/publications/2003/dec/phc-3-20.pdf

U.S. Census Bureau. (2012, July). Louisiana 2010 – Population and Housing units counts (Report No. CPH-2-20). Retrieved from https://www2.census.gov/library/publications/decennial/2010/cph-2/cph-2-20.pdf

U.S. Census Bureau. (2021, August). 2020 Population and Housing State Data. Retrieved from https://www.census.gov/library/visualizations/interactive/2020-population-and-housing-state-data.html

Vahdat-Aboueshagh, H., Tsai, F., (2021). Constructing large-scale complex aquifer systems with big well log data: Louisiana model. *Computers and Geosciences*. 148, 104687. doi:10.1016/j.cageo.2021.104687

Walter, J. I., Dotray, P. J., Frohlich, C., & Gale, J. F. (2016). Earthquakes in northwest Louisiana and the Texas–Louisiana border possibly induced by energy resource activities within the Haynesville shale play. *Seismological Research Letters*. 87(2A), 285-294. doi:10.1785/0220150193

Wheaton, J., Brasington, J., Darby, S., Sear, D., (2010). Accounting for uncertainty in DEMs from repeat topographic surveys: improved sediment budgets. *Earth Surface processes and*

Landforms. 35 (2), 136-156. doi:10.1002/esp.1886 [computer software] https://github.com/Riverscapes/gcd

Wheaton, J., (2018). Principles of topographic change detection. EarthCube Advancing the Analysis of HRT Workshop Advancing the Analysis of High-Resolution Topography, Broomfield, CO. August 21-24. https://www.youtube.com/watch?v=QIoK52W5sUM&ab_channel=OpenTopography (last accessed November 10, 2020)

White, E. (2017). Water Resources of the Southern Hills Regional Aquifer System, Southeastern Louisiana. *U.S. Geological Survey* Fact Sheet 2017–3010. doi:10.3133/fs20173010

Yu, C., Penna, N., Li, Z., (2017). Generation of real-time mode high-resolution water vapor fields from GPS observations. *Journal of Geophysical Research: Atmospheres*. 122, 2008-2025. doi: 10.1002/2016JD025753

Zhong, W., Chu, T., Tissot, P., Wu, Z., Chen, J., Zhang, H., (2022). Integrated coastal subsidence analysis using InSAR, LiDAR and land cover data. *Remote Sensing of Environment*. 282. doi: 10.1016/j.rse.2022.113297

JGR: Earth Surface

Supporting Information for

Variations in subsidence patterns in the Gulf of Mexico passive margin from Airborne-LiDAR data and Time Series InSAR: Baton Rouge Case Study.

Carolina Hurtado-Pulido[1], Reda Amer[2], Cynthia Ebinger[1], Hayden Holcomb[1]

[1]Department of Earth and Environmental Sciences, Tulane University.

[2]St Louis University, St Louis, Missouri

Contents of this file

Tables S1 to S3

Figures S1 to S10

Text T1 and T3

Introduction

Tables S1 and S2 have additional details regarding the LiDAR and SAR data not included in the main text. Table S3 describes the point samples taken for the time series in figures 4 and 5.

Figures S1 to S10 are mentioned in the main manuscript.

Text T1 to T3 are further explanations of data in the main manuscript.

References cited here can be found in the main manuscript.

Table S1:Characteristics for SAR data for ENVISAT and Sentinel-1 (ESA, 2021a, 2021b).

	ENVISAT-ASAR	**Sentinel-1**
Incidence Angle	23° (scene center)	37-39° (center sub-swath 2)
Polarization	Vertical transmit - Vertical receive (VV)	VV
Pixel dimensions (azimuth x range)	5x25 m	14.1x2.3 m
Swath width (km)	5-1150	250
Average coverage along track (km)	100	22.5-22.7
Average coverage across track (km)	56-100	2.7-3.5
Mean Altitude (km)	800	693
Revisit time (days)	35	12
Images used (First and last lines correspond to the start and end of each file in the column list)	ASA_IMS_1PNESA 20040418_161027_000000182026_00083_11159 20040523_161031_000000182027_00083_11660 20050227_161027_000000182035_00083_15668 20050403_161029_000000182036_00083_16169 20060212_161021_000000182045_00083_20678 20060319_161018_000000182046_00083_21179 20070930_161022_000000182062_00083_29195 20071104_161022_000000182063_00083_29696 20071209_161018_000000182064_00083_30197 20080113_161020_000000182065_00083_30698 20080217_161019_000000182066_00083_31199 20080427_161018_000000182068_00083_32201 20080601_161020_000000182069_00083_32702 20080706_161021_000000182070_00083_33203 20081123_161017_000000182074_00083_35207 20081228_161019_000000182075_00083_35708 20090308_161018_000000182077_00083_36710 20100711_161010_000000182091_00083_43724	S1A_IW_SLC__1SDV_ 20170404T000154_20170404T000221_015987_01A5E6_E689 20170428T000155_20170428T000222_016337_01B092_6BCA 20170522T000156_20170522T000223_016687_01BB42_34B3 20170814T000201_20170814T000228_017912_01E0A9_3885 20170919T000202_20170919T000229_018437_01F0B0_A322 20171013T000203_20171013T000230_018787_01FB66_000F 20171106T000203_20171106T000230_019137_020620_3C80 20180105T000201_20180105T000228_020012_022178_B82A 20180210T000200_20180210T000227_020537_02322D_BEC0 20180306T000159_20180306T000226_020887_023D47_EAF0 20180610T000203_20180610T000230_022287_026979_A6AE 20180704T000205_20180704T000232_022637_0273E0_FF2F 20180902T000208_20180902T000235_023512_028F62_FE69 20181113T000209_20181113T000236_024562_02B230_AD1A 20190112T000207_20190112T000234_025437_02D177_FB1A 20190205T000206_20190205T000233_025787_02DE35_6C0A 20190313T000206_20190313T000233_026312_02F101_7AC1 20190325T000206_20190325T000233_026487_02F77B_E583 20190430T000208_20190430T000235_027012_030AA6_7891

	_0000.N1	20190524T000209_20190524T000236_027362_031615_8339 20190629T000210_20190629T000238_027887_032604_1B81 20190723T000212_20190723T000239_028237_033099_4B20 20190828T000214_20190828T000241_028762_0341E0_CA2A 20190921T000215_20190921T000242_029112_034DFB_8DE7 20191027T000216_20191027T000243_029637_03600E_DBC0 20191120T000215_20191120T000242_029987_036C4D_72A0 20191226T000214_20191226T000241_030512_037E76_0DD0 20200131T000213_20200131T000240_031037_0390C2_751B 20200224T000212_20200224T000239_031387_039CE2_AD2E 20200331T000213_20200331T000240_031912_03AF2A_5844 20200424T000213_20200424T000240_032262_03BB79_34AE 20200530T000215_20200530T000243_032787_03CC40_3FB6 20200729T000219_20200729T000246_033662_03E6C3_D4C6 .SAFE

Table S2: Characteristics for LiDAR point clouds from 1999 and 2018.

	1999	**2018**
Instrument	Leica ALS40	Leica ALS70 HP
Altitude (m)	2,438	1,152
Point spacing (m)	4	0.33
Pulse rate (kHz)	15	450
Vertical Accuracy (cm) -RMSE	15	3.6

Table S3: Description of points for samples of InSAR time series in Figures 4C and 5C.

P#	**Number PS Sentinel**	**Number PS EnviSAT**	**Description**
SJB1	32	16	Points over the building where SJB1 is installed
1	75	31	Points over the Life Storage Baton Rouge, built in ~2004.
2	22	0	Points over homes built in ~2007. Near the fault in the northern block.
3	21	3	Points over homes built in ~2017. Near the fault in the northern block.
4	48	19	Points over the Woman's Hospital built in ~2010. Near the fault in the southern block. This hospital did not exist for Envisat, then these points are from complete area that is the hospital nowadays.
5	74	79	Points at a radius of 160 meters to the injection point with serial number 189576.
6	64	0	Points over the Baton Rouge Wastewater Treatment plant built in ~2009.

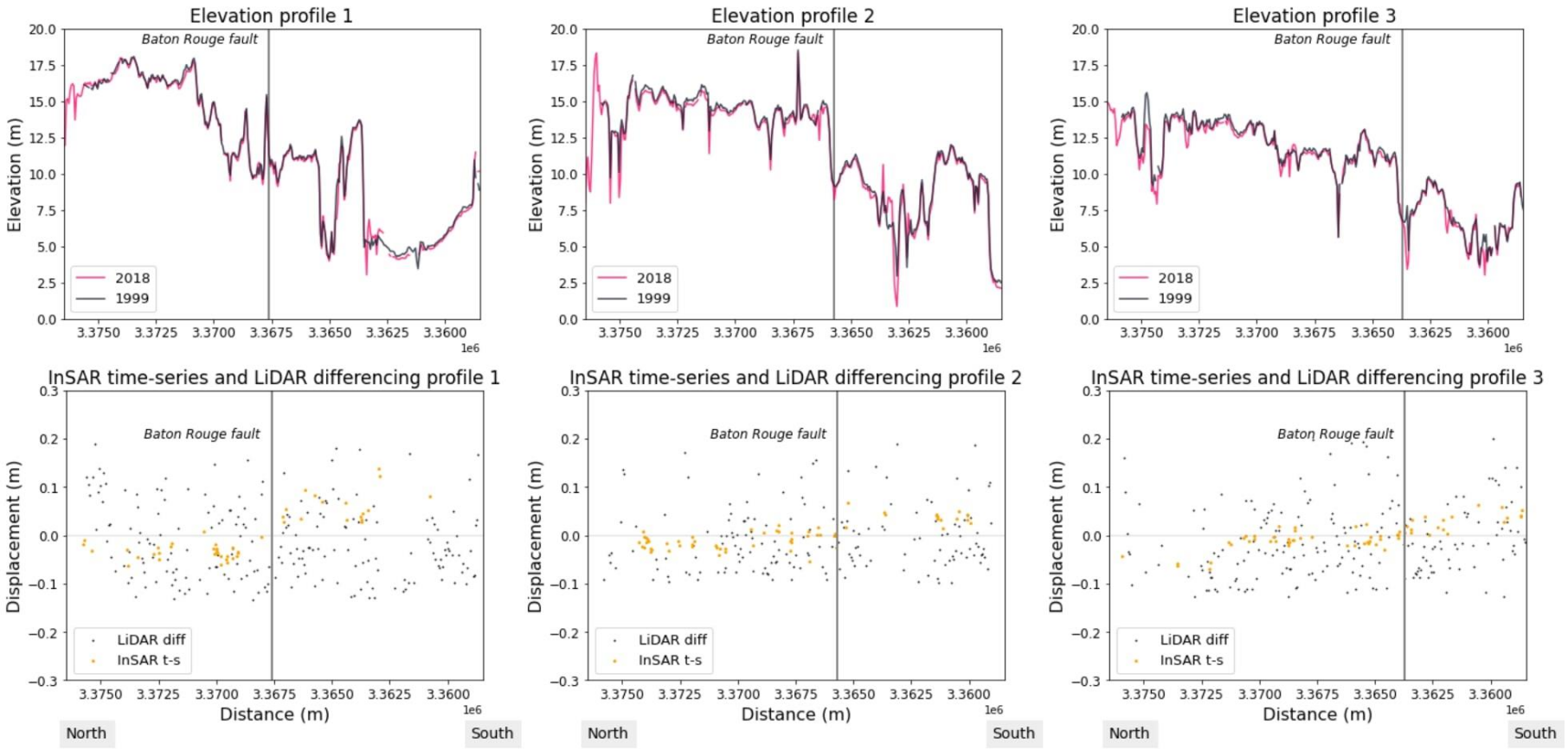

Figure S1: Comparison of elevations using the DEM from 1999 and 2018 in the upper panel and results from our methods along those profiles. For location of the profiles see Figure 2. For the upper profiles, data is averaged every 10 meters from the DEMs, and lower panel is averaged every 20 meters from the LiDAR Vertical difference results (Fig. 8) and the InSAR time-series for Sentinel-1 results (Fig. 4). The time series in the lower panel are not tied to 1LSU reference point.

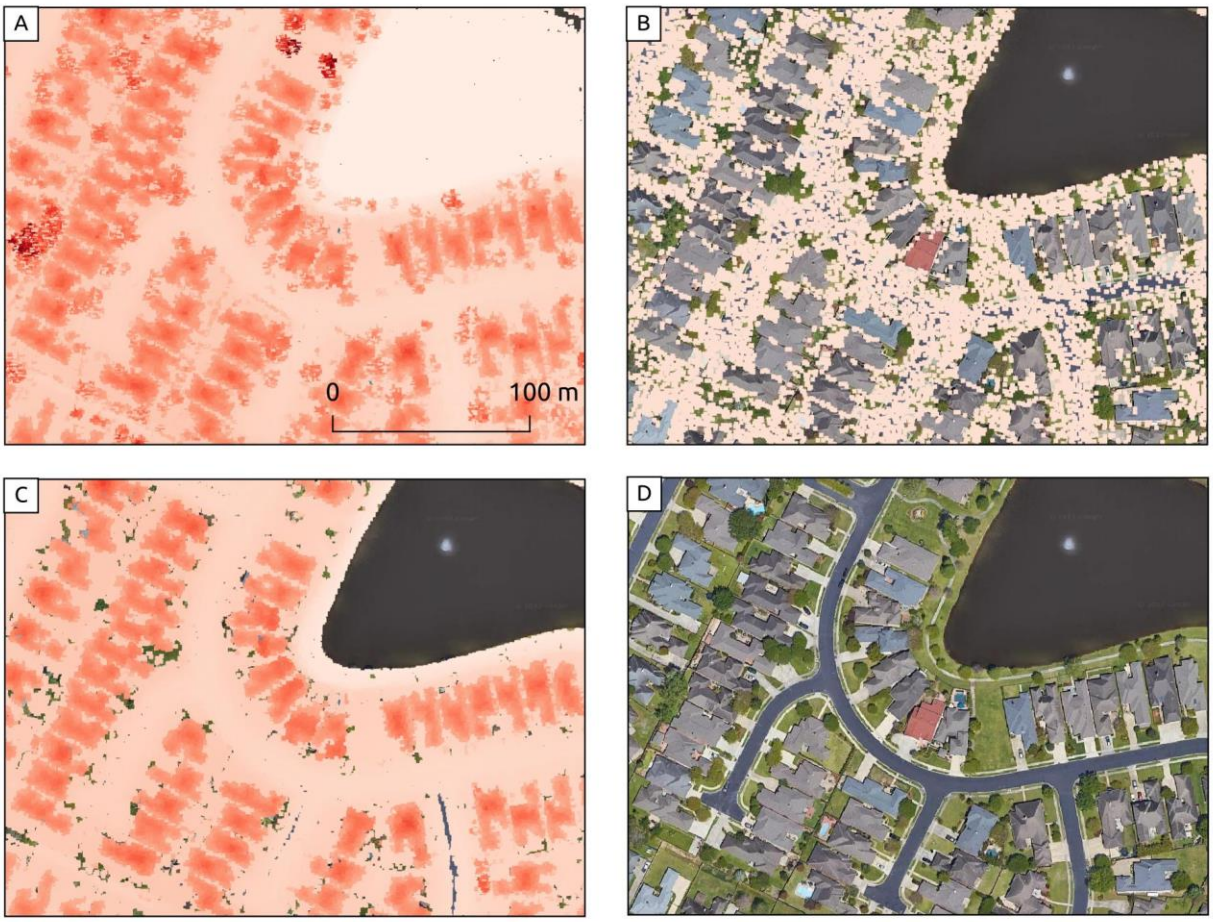

Figure S2: Example of stable surfaces from 2018 LiDAR point cloud. **A)** Original point cloud. **B)** LiDAR points classified by distributor as ground. **C)** Chosen LiDAR points from stable surfaces. **D)** Reference image of the area. Base map imagery from QuickMapServices - QGIS (Map data ©2015 Google).

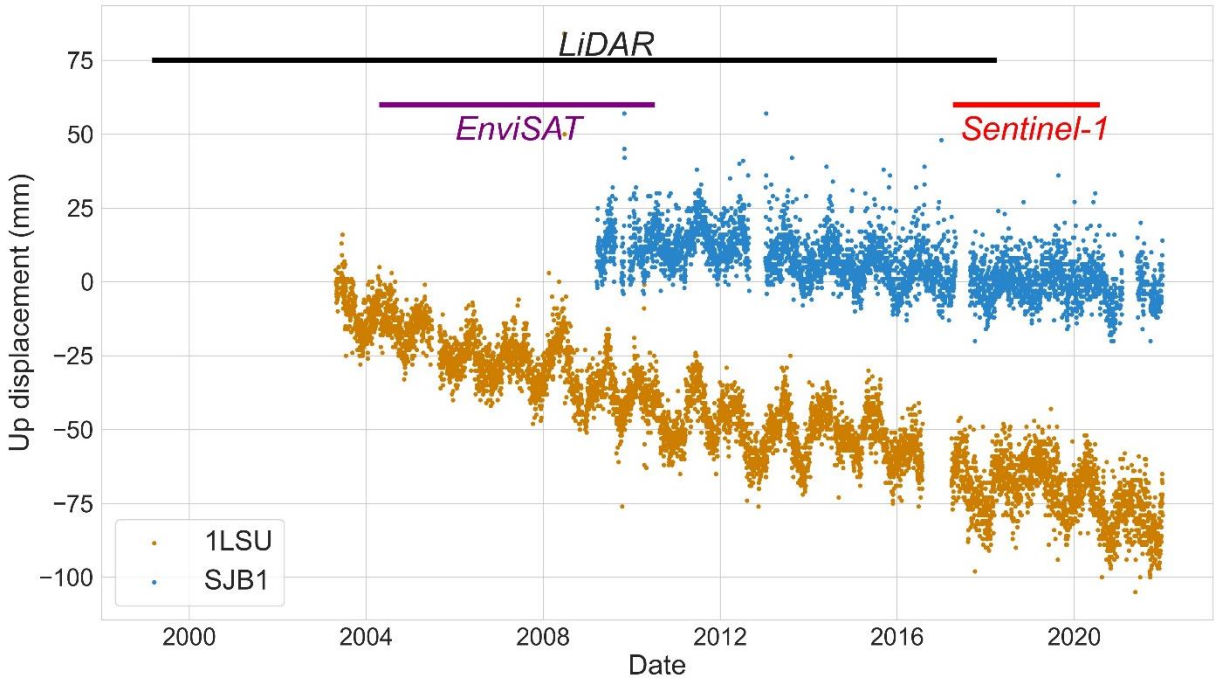

Figure S3: GNSS time series showing the vertical component changes. Horizontal lines labeled as LiDAR, EnviSAT, and Sentinel-1 indicate the time span of these datasets in comparison with the two GNSS time series in the area. GNSS time series are with reference to the fixed North American plate and are from the Nevada Geodetic Survey (Blewitt et al., 2018) and transformed to NAD 83 using the software Horizontal Time-Dependent Positioning from NOAA (Pearson and Snay, 2013).

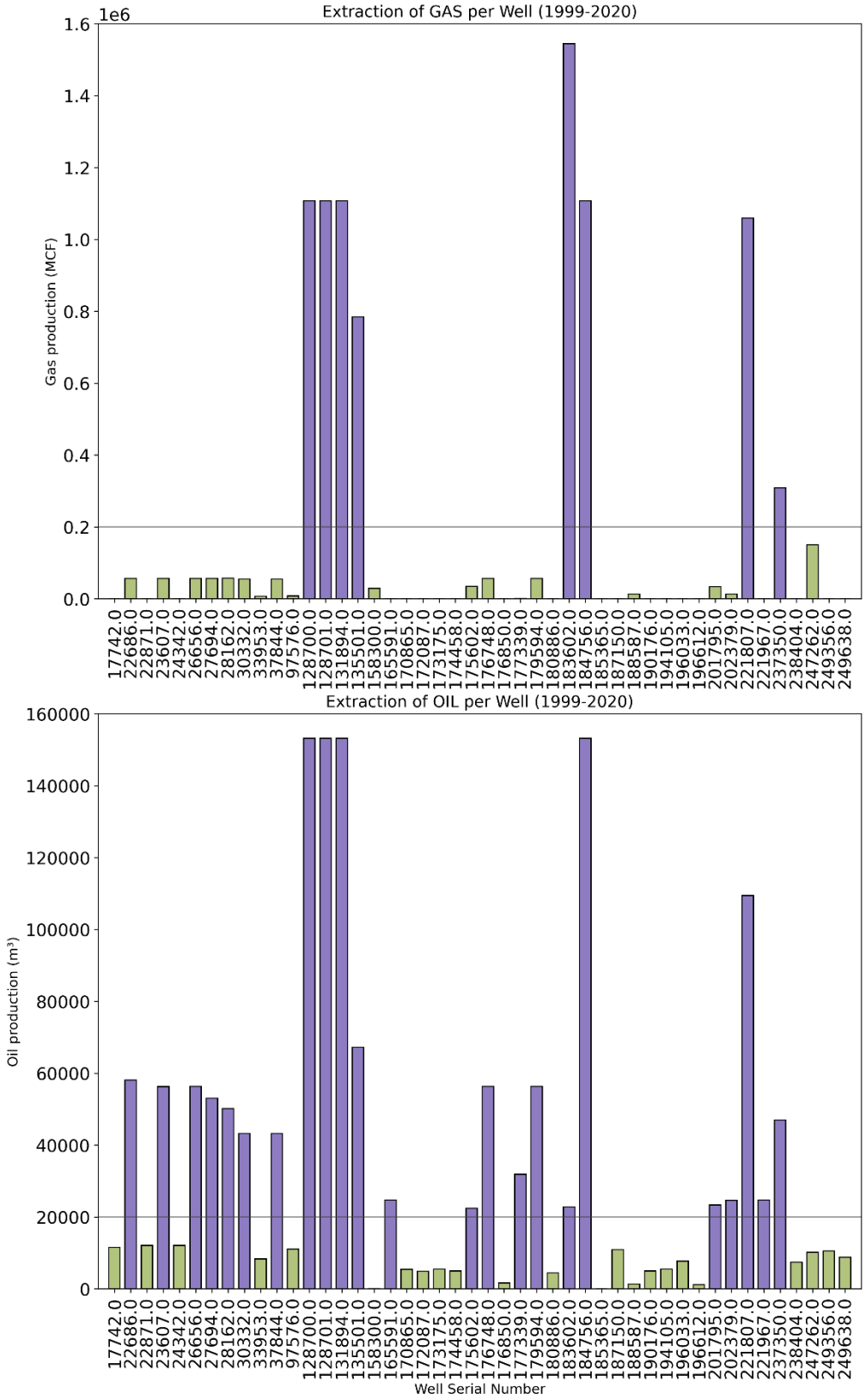

Figure S4: Total gas and oil extracted per well between 1999-2020. Horizontal lines indicate the minimum extraction value to consider a well in our study (200,000 MFC for gas and 20,000 m^3 for oil). Horizontal axis is the well serial numbers. Dark wells extracted more than the threshold value.

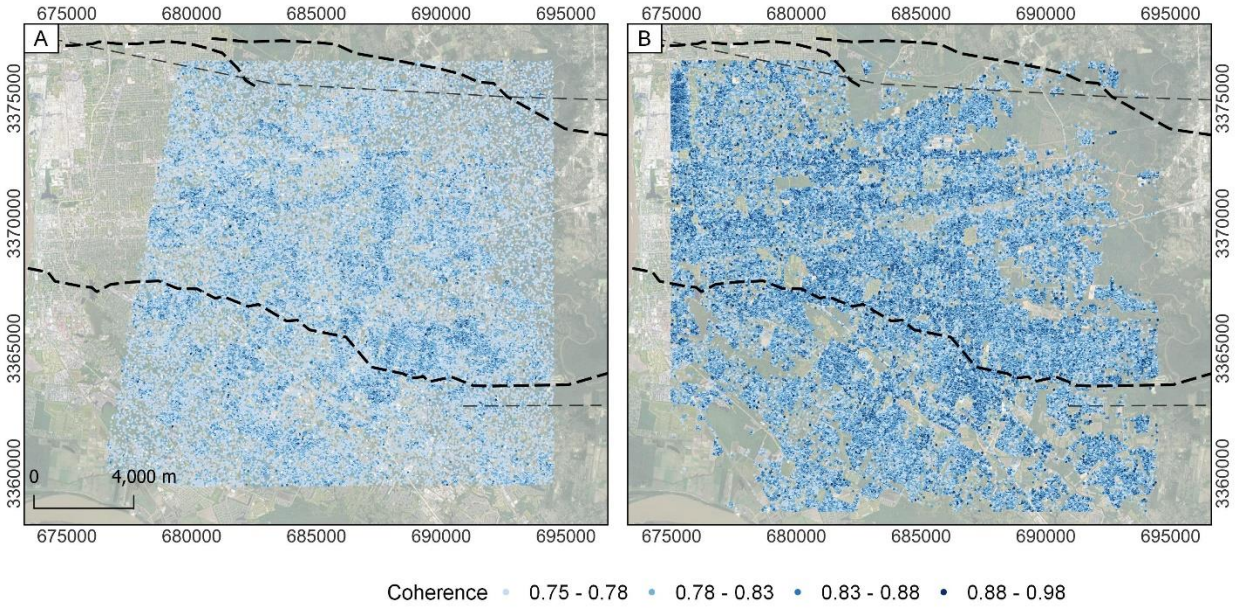

Figure S5: Coherence values for the InSAR time series results. A) EnviSAT coherence for time series between 2004 to 2010, B) Sentinle-1 coherence for time series between 2017 to 2020.

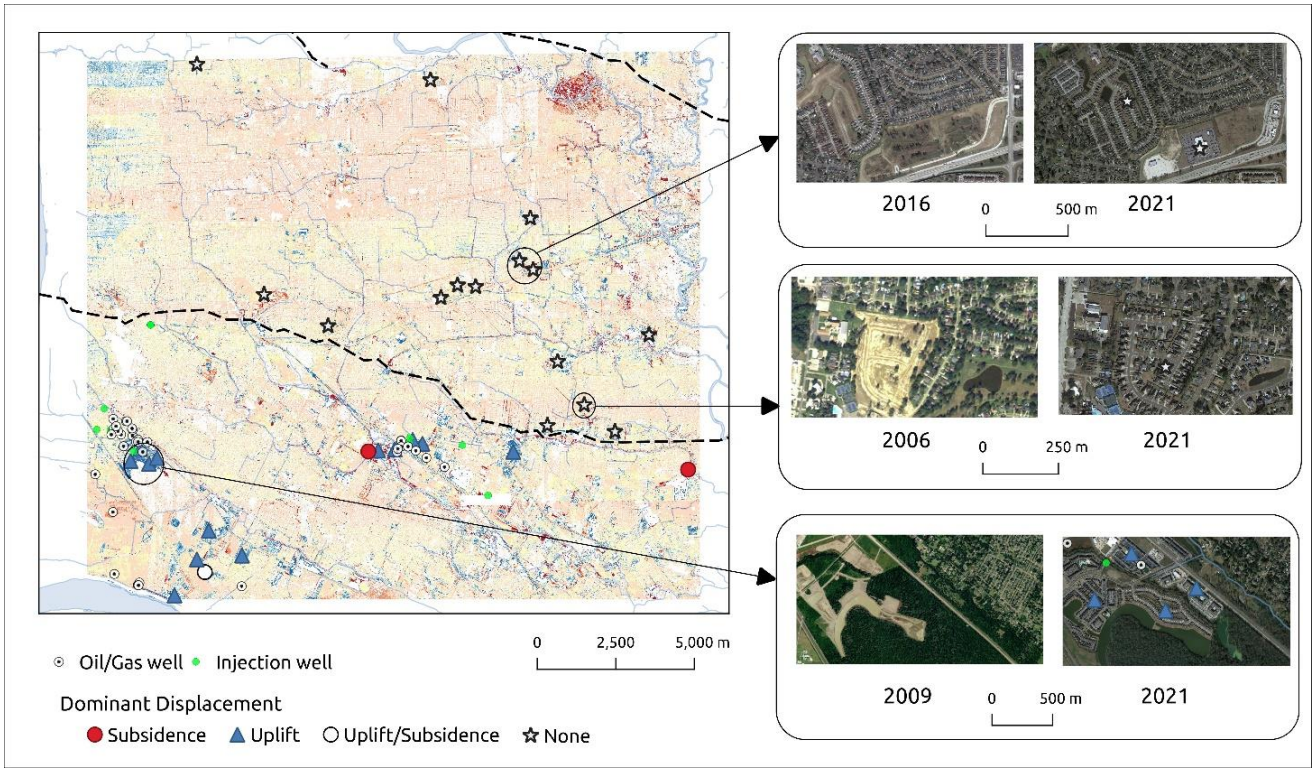

Figure S6: Examples of location of urban constructions built between 1999-2020 and how they look in 2021. Dominant displacement refers to the dominant vertical movement in the area near to the construction. The circle labeled as Uplift/Subsidence encloses the Baton Rouge Wastewater Treatment that encounters uplift to the northwest and subsidence to the southeast. Oil/Gas and injection wells are drawn to compare with building constructions near and far from these wells. Legend for displacement is in Figure 8. Images from 2021 taken from QuickMapServices - QGIS (Map data ©2015 Google). Images from past years are taken from the Historical imagery from Google Earth Pro. Well data from the Louisiana Department of Natural Resources (SONRIS), (n.d.).

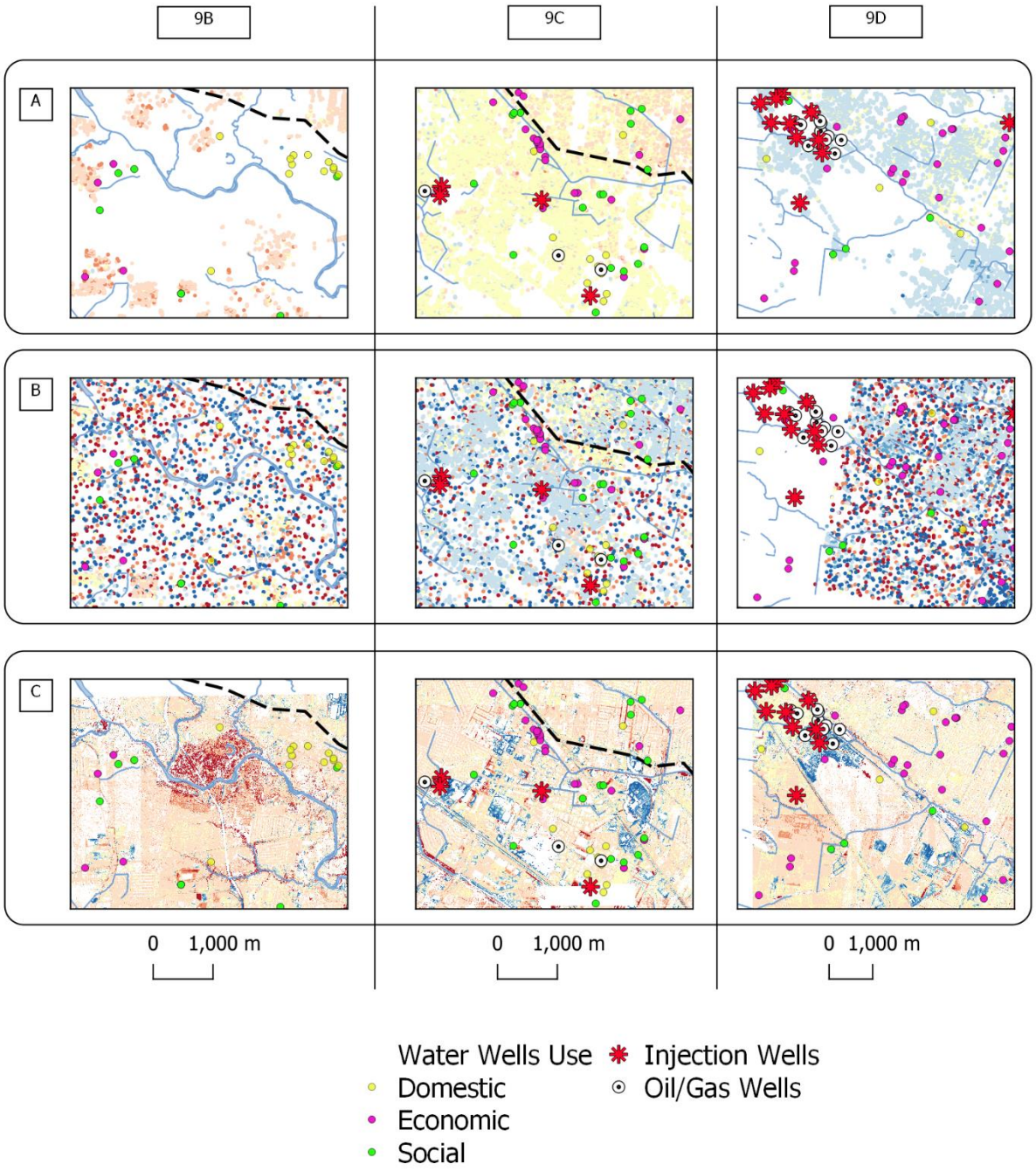

Figure S7: Example of areas experiencing subsidence or uplift determined by different methods compared with injecting and extracting wells. A) Vertical displacement rates calculated with InSAR time series using Sentinel-1 data between 2017-2020. B) Vertical displacement rates calculated with InSAR time series using EnviSAT data between (2004-2010). C) Vertical displacement calculated with LiDAR differencing between 1999-2018. Location of these areas are found in Figure 9. Legend for displacement and rates are in Figures 5 and 9. Well data from the Louisiana Department of Natural Resources (SONRIS), (n.d.)

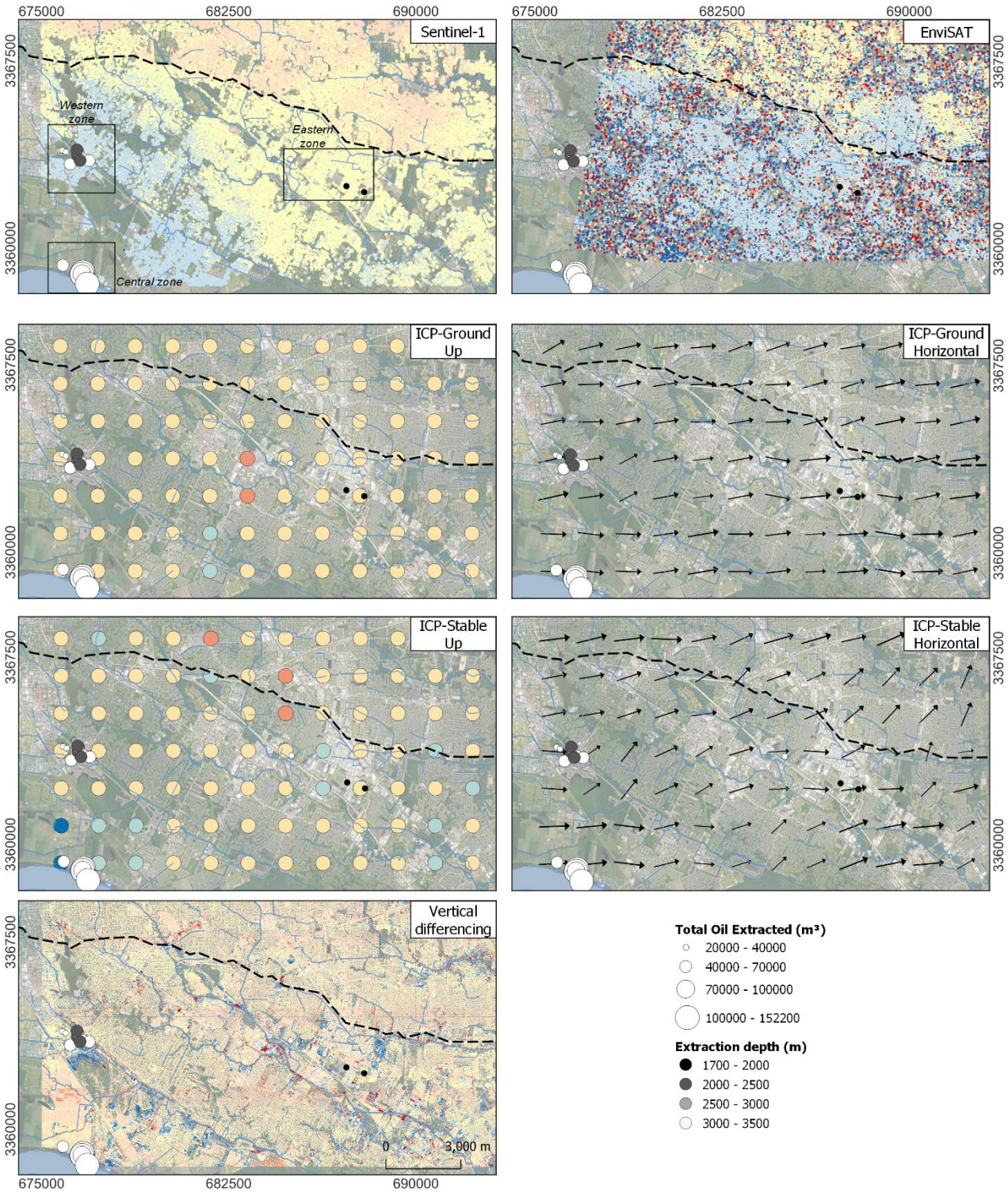

Figure S8: Total oil extracted per well and depth shown in all our results. Method used indicated in the top right corned of each figure.

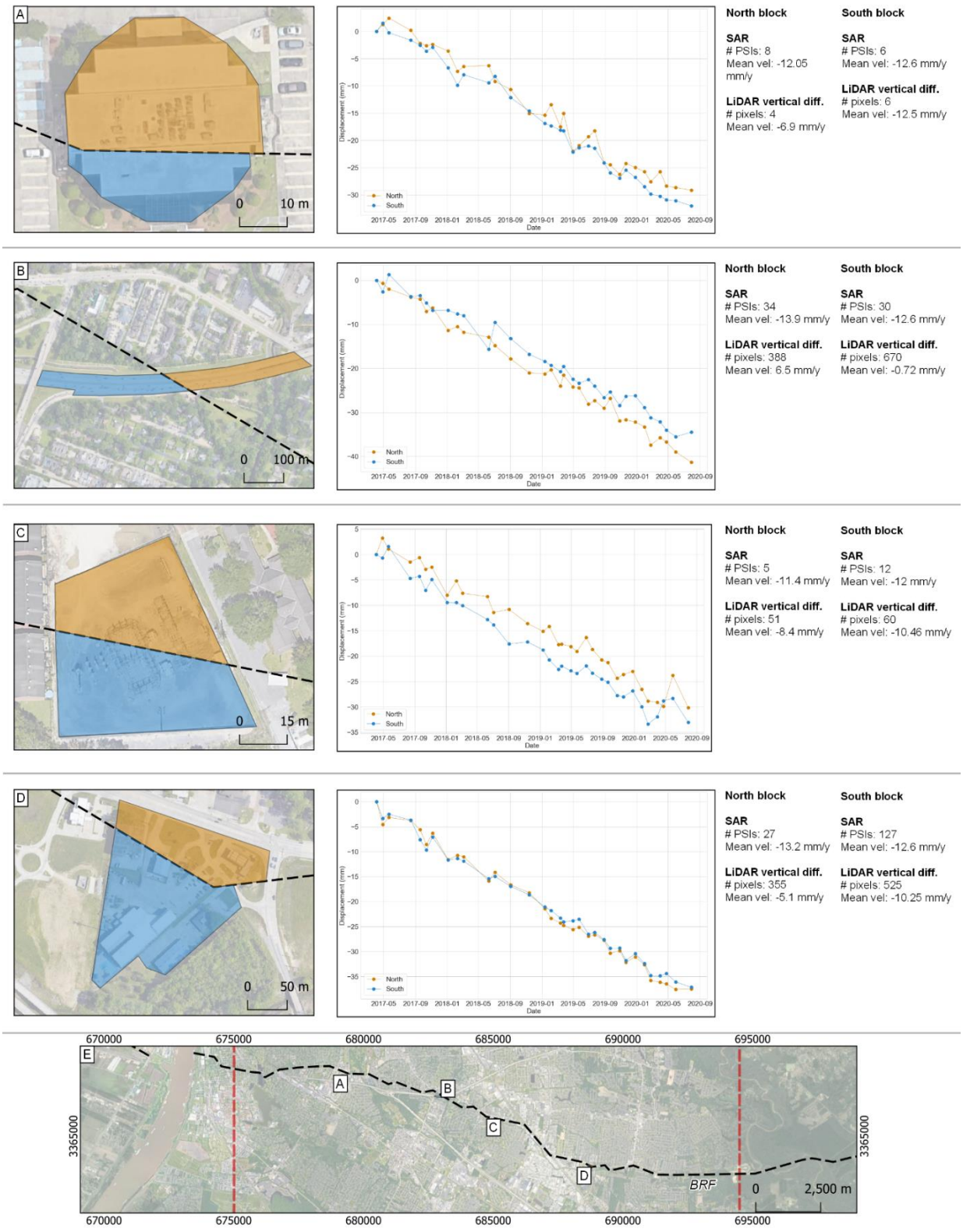

Figure S9: Examples of structures located over the Baton Rouge Fault. The middle column shows the average time series created with the PSIs from Sentinel-1 between 2017-2020 in LOS direction. The right-hand column shows a summary of the results with Sentinel-1 in the LOS direction and LiDAR vertical differencing for the structures. **E)** shows the location of the examples along the Baton Rouge Fault.

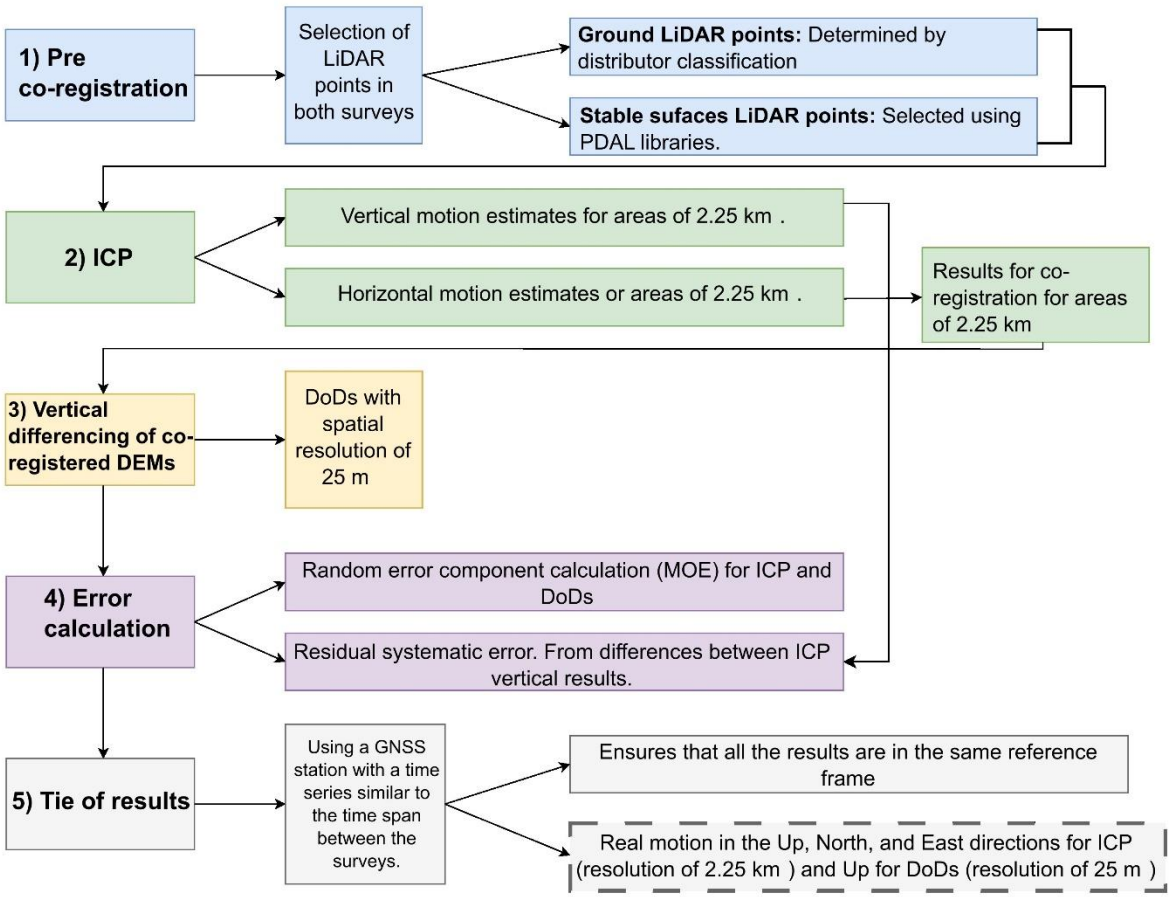

Figure S10: Workflow followed with LiDAR data. Squares with dashed lines indicate results discussed in the text. ICP receives ground LiDAR points and stable surface LiDAR points separately. Details described in the main text.

T1. Brief description of PSI technique with SARscape

The first part of the process is data preparation. It includes co-registration and interferogram generation between the reference image and the other images in the stack, as well interferometric flattening. The topographic phase component is prepared using a DEM to be subtracted from the total interferometric phase. Then, reference points are chosen using the Amplitude Dispersion Index, defined as the temporal average amplitude of a pixel over standard deviation of the amplitude of a pixel**.** Then, the first inversion step is executed. This step calculates displacement velocity and residual height using a linear model for each pixel with respect to the reference points. The model estimates are removed from all the interferograms to recalculate velocity and residual height. Next, the second inversion is applied. At this step the atmospheric phase is estimated to remove spatial and temporal variations from the interferometric phase caused by transmission through the troposphere. SARscape uses water vapor data contained in ENVISAT MERIS, OSCAR (Online Services for Correcting Atmosphere and

Radar), or European Center for Medium-range Weather Forecast (ECMWF) to correct atmospheric disturbances in interferometric pairs. Next, displacements are calculated from the clean interferometric phase for each interferogram. The estimates for displacement and residual heights are recalculated and only pixels with coherence larger than 0.66 are retained. The results are geocoded and exported to raster and vector files (L3Harris, 2014; 2021; Ferretti et al., 2001).

T2. Interpretation S7 - Examples of structures located over the Baton Rouge Fault (BRF)

Here, we present some examples of human-made structures along the BRF. The time series and estimated average for InSAR were calculated using Sentinel-1 data captured between 2017 - 2020 in the LOS direction. LiDAR results correspond to the mean rate motion in the vertical direction calculated using the mean vertical motion that occurred between 1999-2018. The rates calculated with both tools agree in direction but not necessarily in magnitude.

The westernmost structure (Fig. S7-A) shows that the northern block is moving slightly slower than the southern block in the LOS direction, although the results from LiDAR vertical differencing show a large difference between the northern and the southern block of the BRF. The structures in the middle (Fig. S7 – B and C) show more differences between the northern and southern blocks of the fault. Structure B (Highway I-12) shows that the northern block is subsiding faster than the southern block. This persists in the LiDAR results but in this case, the rates are more positive. Structure C shows that the southern block is moving faster than the northern area. It is important to highlight B and C because this area may have more dramatic changes but with opposite creep direction. Finally, the easternmost structure (S7-D) has almost the same motion through time but there are important differences from the LiDAR results.

T3. Empirical tropospheric error estimation with GACOS data

To provide an approximation of the tropospheric delay across the area we present the variation for each interferogram of the time series. We estimate the delay for each interferogram following the instructions included with the GACOS dataset (steps 1 and 2).

1) Tropospheric delay estimated for the EnviSAT time series between 2004-2010 from GACOS data. The average range for the tropospheric delay is 28.75 mm with a standard deviation of 19.26 mm.

Interferogram	Min (mm)	Max (mm)	Range (mm)
200405_200404	-6.0806	2.7735	8.8541
200502_200405	-8.7674	4.7374	13.5048
200504_200502	-4.6723	11.5664	16.2387
200602_200504	-0.6644	0.9008	1.5652
200603_200602	-7.0457	12.4636	19.5093
200709_200603	-37.5965	19.1503	56.7468
200711_200709	-19.4143	39.6906	59.1049
200712_200711	-21.7647	10.5462	32.3109
200801_200712	-1.5267	5.68785	7.21455
200802_200801	-29.2549	17.4207	46.6756
200804_20080217	-19.9467	29.1889	49.1356
200806_200804	-8.35941	16.587	24.94641
200807_200806	-21.7957	12.8036	34.5993
200811_200807	-3.22485	6.35338	9.57823
200812_200811	-18.966	7.65491	26.62091
200903_200812	-18.033	41.5432	59.5762
201007_200903	-16.3195	6.26377	22.58327

2) Tropospheric delay estimated for the Sentinel-1 time series between 2017-2020 from GACOS data. The average range for the tropospheric delay is 35.95 mm with a standard deviation of 18.17 mm.

Interferogram	Min (mm)	Max (mm)	Range (mm)
201704_20170404	-34.0123	10.705	44.7173
201705_201704	-3.46327	19.7599	23.22317
201708_201705	-22.4526	7.8857	30.3383
201709_201708	-5.21444	27.2379	32.45234
201710_201709	-21.4207	9.04634	30.46704
201711_201710	-10.0887	27.6888	37.7775
201801_201711	-5.775	4.51609	10.29109
201802_201801	-9.5724	4.3882	13.9606
201803_201802	-3.0615	21.236	24.2975
201806_201803	-63.766	22.7534	86.5194
201807_201806	-20.4899	49.1851	69.675
201809_201807	-11.0901	10.5169	21.607
201811_201809	-45.635	16.9375	62.5725
201901_201811	-13.6741	39.8819	53.556
201902_201901	-7.68975	7.28437	14.97412
201903_20190313	14.6795	41.2784	26.5989
20190313_20190205	-43.7655	-17.7109	26.0546
201904_201903	-10.0052	15.6866	25.6918
201905_201904	-17.5176	17.7894	35.307
201906_201905	-13.1707	33.0668	46.2375
201907_201906	-33.3431	10.1202	43.4633

201908_201907	-16.5706	23.2875	39.8581
201909_201908	-15.7881	33.9224	49.7105
201910_201909	-4.57821	7.00345	11.58166
201911_201910	-13.0012	6.253	19.2542
201912_201911	-9.38396	13.3874	22.77136
202001_201912	-25.4836	12.6421	38.1257
202002_202001	-8.30461	14.7302	23.03481
202003_202002	-14.4527	42.9988	57.4515
202005_202003	-44.6926	15.8424	60.535
202007_202005	-9.9665	22.3449	32.3114